

# REPORT DOCUMENTATION PAGE

*Form Approved*  
OMB No. 0704-0188

Public reporting burden for this collection of information is estimated to average 1 hour per response, including the time for reviewing instructions, searching data sources, gathering and maintaining the data needed, and completing and reviewing the collection of information. Send comments regarding this burden estimate or any other aspect of this collection of information, including suggestions for reducing this burden to Washington Headquarters Service, Directorate for Information Operations and Reports, 1215 Jefferson Davis Highway, Suite 1204, Arlington, VA 22202-4302, and to the Office of Management and Budget, Paperwork Reduction Project (0704-0188) Washington, DC 20503.

**PLEASE DO NOT RETURN YOUR FORM TO THE ABOVE ADDRESS.**

1. REPORT DATE (DD-MM-YYYY)  April 30, 2009	2. REPORT TYPE  Final Performance Report	3. DATES COVERED (From - To)  2/15/06 to 1/31/09		
4. TITLE AND SUBTITLE  Site Directed Nucleation and Growth of Ceramic Films on Metallic Surfaces		5a. CONTRACT NUMBER  FA9550-06-0-0133		
		5b. GRANT NUMBER  N/A		
		5c. PROGRAM ELEMENT NUMBER		
6. AUTHOR(S)  D.C. Hansen, A.S. Mount and K.M. Hansen		5d. PROJECT NUMBER		
		5e. TASK NUMBER  01		
		5f. WORK UNIT NUMBER		
7. PERFORMING ORGANIZATION NAME(S) AND ADDRESS(ES)  University of Dayton Research Institute, 300 College Park, Dayton, OH 45469-01309 Clemson University, Dept. of Biological Sciences, Clemson SC 29634		8. PERFORMING ORGANIZATION REPORT NUMBER  UDR-TR-2009-69		
9. SPONSORING/MONITORING AGENCY NAME(S) AND ADDRESS(ES)  Air Force Office of Scientific Research/NL 801 North Randolph Street, Room 732 Arlington, VA 22203-1977		10. SPONSOR/MONITOR'S ACRONYM(S)		
		11. SPONSORING/MONITORING AGENCY REPORT NUMBER  AFRL-AFOSR-VH-TR-2016-0607		
12. DISTRIBUTION AVAILABILITY STATEMENT  Please withhold the distribution of this Final Report for one year, to allow for complete publication of the discussed results in peer-reviewed journal publications, then Distribution Statement A				
13. SUPPLEMENTARY NOTES				
14. ABSTRACT: The biomineralization and shell formation in the Eastern oyster ( <i>Crassostrea virginica</i> ) has been elucidated involving a previously unknown cellular-mediated process. Laboratory studies have confirmed that circulating immune blood cells (hemocytes) are directly involved in oyster shell formation, where two mineralized layers of shell are deposited in conjunction with an extracellular macromolecular complex (EMC) membrane. The EMC functions as an intelligent surface providing information that helps cells orchestrate the next layer of crystalline composite formation. The deposition and growth by cells of these nanoscale composite organic/mineral layers <i>in situ</i> on metal alloy substrates and the deposition of nanometer sized ceramic crystals onto metallic surfaces ( <i>ex vivo</i> ) have been achieved. The bioceramic shell has also been investigated to determine its physical and chemical composition, its electrochemical properties and thermal behavior. Analysis reveals this biocomposite material to be composed of numerous incongruent layers of different chemical composition and porosity. Conductivity within the pores is dependent on the ionic concentration of the electrolyte, suggesting that the tortuosity across the shell material has an effect on the transport of ions. The surface charges within the pores of the shell material facilitate the conduction of ions, much like a ceramic membrane.				
15. SUBJECT TERMS				
16. SECURITY CLASSIFICATION OF:  a. REPORT UNCLASSIFIED		17. LIMITATION OF ABSTRACT  Same as Report	18. NUMBER OF PAGES	19a. NAME OF RESPONSIBLE PERSON  19b. TELEPHONE NUMBER (Include area code)
b. ABSTRACT UNCLASSIFIED				
c. THIS PAGE UNCLASSIFIED				

## **AFOSR Final Performance Report**

**Project Title:** SITE DIRECTED NUCLEATION AND GROWTH OF CERAMIC FILMS ON METALLIC SURFACES.

**Award Number:** FA9550-06-1-0133

**Start Date:** Feb 15, 2006

**Program Manager:** Major Michelle E. Ewy (Rauch) , Ph.D.  
Program Manager  
Aerospace, Chemical, and Material Sciences Directorate  
Air Force Office of Scientific Research  
875 North Randolph St  
Suite 325, Room 4111  
Arlington, VA 22203  
Phone: (703) 696-7297  
Fax: (703) 696-8451

**Principal Investigator:** Douglas C. Hansen  
Materials Engineering Division  
University of Dayton Research Institute  
300 College Park  
Dayton, OH 45469-0130  
E-mail: [Douglas.Hansen@udri.udayton.edu](mailto:Douglas.Hansen@udri.udayton.edu)  
Phone: (937) 229-2517  
Fax: (937) 229-2503

**Co-Investigators**

Prof. Andrew S. Mount  
Clemson University  
Dept. Biological Sciences  
132 Long Hall  
Clemson, S.C. 29634  
E-mail: [mount@clemson.edu](mailto:mount@clemson.edu)  
Phone: (864) 656-3597

Karolyn M. Hansen  
Materials Engineering Division  
University of Dayton Research Institute  
300 College Park  
Dayton, OH 45469-0130  
E-mail: [Karolyn.Hansen@udri.udayton.edu](mailto:Karolyn.Hansen@udri.udayton.edu)  
Phone: (937) 229-2141  
Fax: (937) 229-2503

### **Accomplishments/New Findings:**

- A *cellular based* bioceramic coating material that is produced at ambient temperature and pressure has been described using the Eastern oyster, *Crassostrea virginica* as a model system.
- The cells are capable of depositing crystals and constructing polycrystalline assemblies on different metal surfaces such as AA2024-T3, AA7075-T6, Ti6Al4V and 316L alloys.
- The bioceramic material has been determined to include nanoscale folia, prismatic crystalline structures and organic membranes.
- The foliated layers of the natural oyster shell material have higher O/Ca and C+O ratios than the prismatic layers, suggesting an organization of mineralization during the deposition process.
- Electrochemical Impedance Spectroscopy (EIS) data indicate that the impedance and resistance of the shell material is related to composition of layers more than overall thickness.
- The shell material exhibits a range of impedances from  $10^5$  to  $10^8$  ohms-cm<sup>2</sup>, suggesting that bioengineering of the layer composition could yield ceramic material of varying impedance and capacitance properties.
- Diffusion behavior and pore conductivities are dependent upon electrolyte ion concentration, even though the layers of the material are incongruent, indicating the material (organic polymer and mineral phases) facilitates ionic conduction.
- Thermal transport of the shell material is approximately one order of magnitude higher than glass and one order of magnitude lower than aluminum oxide, suggesting that this material may have applications in aerospace thermal management or fuel cell membranes.

### **Summary:**

Animals of the Phylum Mollusca produce a variety of beautiful and intricately designed calcium carbonate shells. The manner in which these shells are produced by the organism has fascinated researchers for decades. Early research on molluscan shell formation focused primarily on descriptive elements – color, size, structure, component materials (organic versus inorganic), rate of production, crystal structure, and elemental composition. More recent (the past 25 years) research efforts have focused on elucidating the actual mechanism of shell formation and the advent of molecular biology

has facilitated identification of specific proteins and genes involved in crystal and shell formation. Much information on shell formation is still unknown, however, particularly the specific mechanisms of crystallization and the composition and influence of sclerotized organic matrix scaffolding on the structural integrity of mollusc shells.

Using bivalve cupped oysters of the genus *Crassostrea* as a model, shell formation generally occurs at two discrete locations in the organism: 1. the growing outer margin of the shell, and 2. the internal surface of the shell. Shell growth in both areas is initiated by a specific tissue called the *mantle* which encases the soft oyster body and separates it from the surrounding shell. The structure of the mantle margin is tri-lobed with an inner *pallial* lobe, middle *sensory* lobe and outer *shell* lobe. The groove separating the outer and middle lobes is called the *periostracal groove* and is the site for production of the proteinaceous *periostracum* upon which the prismatic calcium carbonate crystals grow. This sclerotized proteinaceous sheet adheres to the underlying shell and effectively restricts exposure of the inner surface of the sheet to the mucous-filled *extrapallial space* between the oyster body and the outer shell. Circulating blood cells (hemocytes) migrate from the oyster open circulatory system onto the forming organic film and deposit calcium carbonate crystals at specific locations. Shell calcium carbonate crystal morphology is species specific and occurs in three crystal types: aragonite, calcite, and vaterite; molluscan shells are composed generally of calcite and aragonite as vaterite is often transient under ambient conditions. *Crassostrea* sp. shells are composed of three types of crystal structure: prismatic (columnar) calcite (on the periostracal sheet at the growing margin), foliated (lath-like) calcite (on the internal surfaces of the shell), and myostracal prismatic aragonite (site of adductor muscle attachment to shell). Prismatic calcite is the crystal form associated with the periostracum, while the foliated calcite is the primary structure of the remainder of the shell. As the organism grows the foliated calcite is formed on top of the thin layer of underlying prismatic calcite. Both foliated and prismatic shell layers have constituent organic matrices which may provide chemical cues for specific localization of crystal deposition by crystal-bearing hemocytes.

As a result of this funded effort, much progress has been made towards understanding the involvement of cellular biomineralization by hemocytes (refractive granulocytes, or REF cells) in the Eastern oyster *Crassostrea virginica*. We have devised a mineralization model based on the results generated during the past 3 years which includes specific spatial and temporal control of hemocyte-mediated crystal nucleation and crystal growth on an underlying organic matrix. This effort has been the result of collaborative research between Dr. A.S. Mount of Clemson University (CU) and Drs. D.C. Hansen and K.M. Hansen of the University of Dayton Research Institute (UDRI). The CU group has focused on the cellular aspects of the biomineralization process, whereas the UDRI group has focused on the interaction of the cells with the substrate metals and the materials science aspect of the natural oyster shell material.

During our three years of AFOSR funding, we have confirmed that circulating immune blood cells (hemocytes) are directly involved in oyster shell formation, where two mineralized layers of shell (prismatic and foliated) are deposited in conjunction with

an organic polymer matrix. The key steps in layered shell formation that have been determined are: 1) secretion of an organic matrix film for cells to adhere; 2) migration of cells onto this membrane to form a mineralization front; 3) deposition of nanocrystals of intracellular origin by specialized cells; 4) formation of polycrystalline assemblies within cellular agglomerations; 5) epithelial directed growth of polycrystalline assemblies to form a uniform mineralized layer; 6) subsequent secretion of second organic matrix film onto the mineralized layer. The polymeric organic films may serve an organizing function such as to inform cells where and when to deposit calcite and may serve to delineate crystal structure.

These results challenge the prevailing shell formation paradigm which holds that shell components (calcium carbonate and organic matrix) are secreted in a complex milieu and that assembly into calcium carbonate (aragonite and calcite) shell layers is matrix-mediated. The paradigm shift is this: *initiation and control of molluscan biomineralization is a cellular process*. Using this knowledge, the deposition and growth by cells of these nanoscale composite organic/mineral layers inside the organism (*in situ*) on metal alloy substrates as well as the deposition of nanometer sized ceramic crystals onto metallic surfaces outside of the organism (*ex vivo*) have been achieved. The determination of the cellular processes involved in shell formation will revolutionize the field of ceramics and other nanoscale composite materials research with the ultimate goal being the cell-free, nanocrystalline assembly of adaptive bioceramic material systems.

The ability to control or determine the degree of porosity of a ceramic material could lead to: engineered porous or non-porous ceramic materials that can be applied without using high temperatures; finely engineered ceramic membranes and ceramic material that can be doped with metal ions in the matrix to make a composite/hybrid material for either semiconductor or catalyst applications; smaller pores for bio-functionality or synthetic bone; the growth of ceramic material around a scaffold/template that would result in components having increased strength:weight ratios for high temperature or high wear environments. Other applications/technology developments for this research include adaptive materials, wear-resistant coatings, and optical coatings and gratings, and many other future novel systems that can change how the Air Force operates in the future.

#### **Cellular Orchestration in Fabrication of Biomineralized Nanocrystalline Composites in the Eastern Oyster, *Crassostrea virginica***

(A.S. Mount, M. Johnstone, N.V. Gohad, Clemson University; K.M. Hansen and D.C. Hansen, UDRI)

**Objective:** Determine the incubation/exposure time parameters between substrates and crystal forming cells for deposition of crystals by oyster hemocytes and investigate and characterize the interface between the deposited crystals, organic coating and substrates.

The phylum Mollusca is unmatched in the mastery of nano-engineered shell microstructures, producing shells that are visually elegant and structurally complex. The resistance to fracture forces and the over-all toughness make these materials ideal models

upon which to devise novel advanced ceramics.<sup>1</sup> Shell formation in the Eastern oyster, *Crassostrea virginica*, is a cell-driven nanoscale process that involves hemocytes (blood cells) and the outer mantle epithelial cells (OME) of the mantle organ.<sup>2-4</sup> The resultant bio-nanocomposite is composed of crystals embedded in a pericellular macromolecular complex (PMC) comprised of proteins, peptides, lipids and carbohydrates.<sup>5</sup> Here we describe the cellular orchestration of nanoscale shell composites on metal alloy implants observed occurring directly at the mineralization front. Our findings suggest that the principal evolutionary innovation of Mollusca is the nanoscale control of shell formation through the mechanism of cellular orchestrated assembly. This form of control enables the simultaneous production and self-organization of organic and mineralized phases resulting in the extraordinarily strong nanocrystalline ceramic.

Oyster shell is a multi-layered composite primarily composed of calcite and about 1% PMC.<sup>6</sup> Two primary layers of shell microstructures are formed. A thin prismatic layer (~100 µm thickness) forms the outer shell layer and is comprised of adjacently positioned columnar, polycrystalline prisms enveloped in PMC. The prisms are oriented such that the long axis is perpendicular to the shell surface. An inner foliated layer forms 90% of shell mass and is comprised of PMC and flattened, regularly shaped crystal units oriented with their long axes parallel to the plane of the shell which coalesce to form sheets or lamina.<sup>7</sup> Both layers are initiated with the delivery of calcite nanocrystals of intracellular origin to the site of shell formation (mineralization front) by refractive (REF) hemocytes.<sup>2</sup> The first event necessary for biomineralization is the provision of a substrate upon which cells can adhere. The oyster accomplishes this task by the secretion of an organic periostracal membrane from specialized epithelial cells located in the mantle organ of the mollusk.<sup>3,8,9</sup>

Most published accounts of shell formation have relied on post hoc observations of previously formed shell layers so little is known about the cellular aspects of the process. Without detailed observations at the mineralization front, the origin and role of the PMC in shell layer formation has remained speculative and elusive. In the present study, we observed PMC formation and cellular activity during oyster shell layer formation by observing folia and prismatic development on different metal alloy surfaces (Ti6Al4V, 7075-T6 aluminum, and 316L stainless steel). This was accomplished by placing metal implants onto particular regions of the shell following notching. By cutting a notch in the shell margin, an inflammatory response, reminiscent of vertebrate and invertebrate wound repair, can be induced. This response results in a numerical increase of REF cells from 5 to 15% of the total hemocyte population, infiltration of hemocytes and secretion of collagen at the mineralization front, and rapid deposition of prismatic and foliated layers into the notched region.<sup>2,10,11</sup> We observed that a prismatic layer preferentially deposited on metal implants inserted along the shell margin while foliated layers form on implants placed between the shell and the mantle organ near the myostracum (the site of adductor muscle attachment). In either case, hemocytes are present at the mineralization front of both layers.

During the initial stages of prismatic layer deposition on 316L stainless steel alloy, the mantle covers the metal surface extending to the shell margin. Within hours, a

flexible membrane forms on the metal surface conforming to the shape of the overlying mantle. Subsequently, this membrane calcifies into a ring pattern corresponding to the pulsed extension/retraction action of the mantle organ during active biominerization (Fig. 1a). The deposited mineral resembles calcite of the prismatic layer. When viewed with epi-fluorescent light microscopy (Nikon AZ-100) in the FITC channel, the auto-fluorescent PMC “walls” surrounding each individual prism are visible (Fig. 1a top inset). Polarized light microscopy reveals the birefringent polycrystalline calcite prisms (Fig. 1a, bottom inset). In Figure 1b, SEM shows that this layer is comprised of 10-25  $\mu\text{m}$  hexagonal prisms coated by a wrinkled membrane, characteristic of prismatic shell.<sup>2,12,13</sup> In addition, concentric imprints are visible at the prism centers (Fig. 1b, black arrow) which appear to be the negative casts of the apical ends of the underlying mantle epithelial cells (Fig. 1c, yellow arrow). The PMC walls appear to originate from the OME (Fig 1c, red arrow). This suggests that there is a 1:1 correspondence of a single prism to that of individual OME cells which is further supported by an analysis of the PMC walls on the surface of the OME. (Fig. 1d-1f). The PMC walls extend through the OME to the depth of the basal lamina (Fig. 1f).<sup>3</sup>

PMC membrane “walls” are fully infiltrated with hemocytes at two locations: on the OME at the mineralization front (Fig. 2a-d) and at the point of substrate contact (Fig. 2e). Cells were not detected within the walls due to the presence of mineral (Fig. 2b and 2f). Hemocytes at both fronts disgorge lipid bound vesicular products (Fig. 2d, white arrow) which associate with the PMC walls (Fig. 2b, 2c, 2d). These cells also disgorge vesicular calcite crystals at the mineralization front (Fig. 2e, white arrow).<sup>2</sup> Individual calcite prisms are visible within the PMC walls on the living tissue (Fig. 2f, arrows).

In the case of folia deposition, our studies reveal that folia formation initiates with the deposition of cell derived exosome-like vesicles in association with a PMC membrane. Some of these vesicles contained CaCO<sub>3</sub> nanocrystals. All of these structures interact simultaneously to form a crystalline composite, thus crystals and membranes are formed as one cohesive unit. Furthermore, given the fact that exosomal vesicles are derived from cell plasma lipid membranes (which are imbued with cell signaling entities),<sup>14</sup> we suggest that the pericellular macromolecular complex (PMC) functions as an intelligent

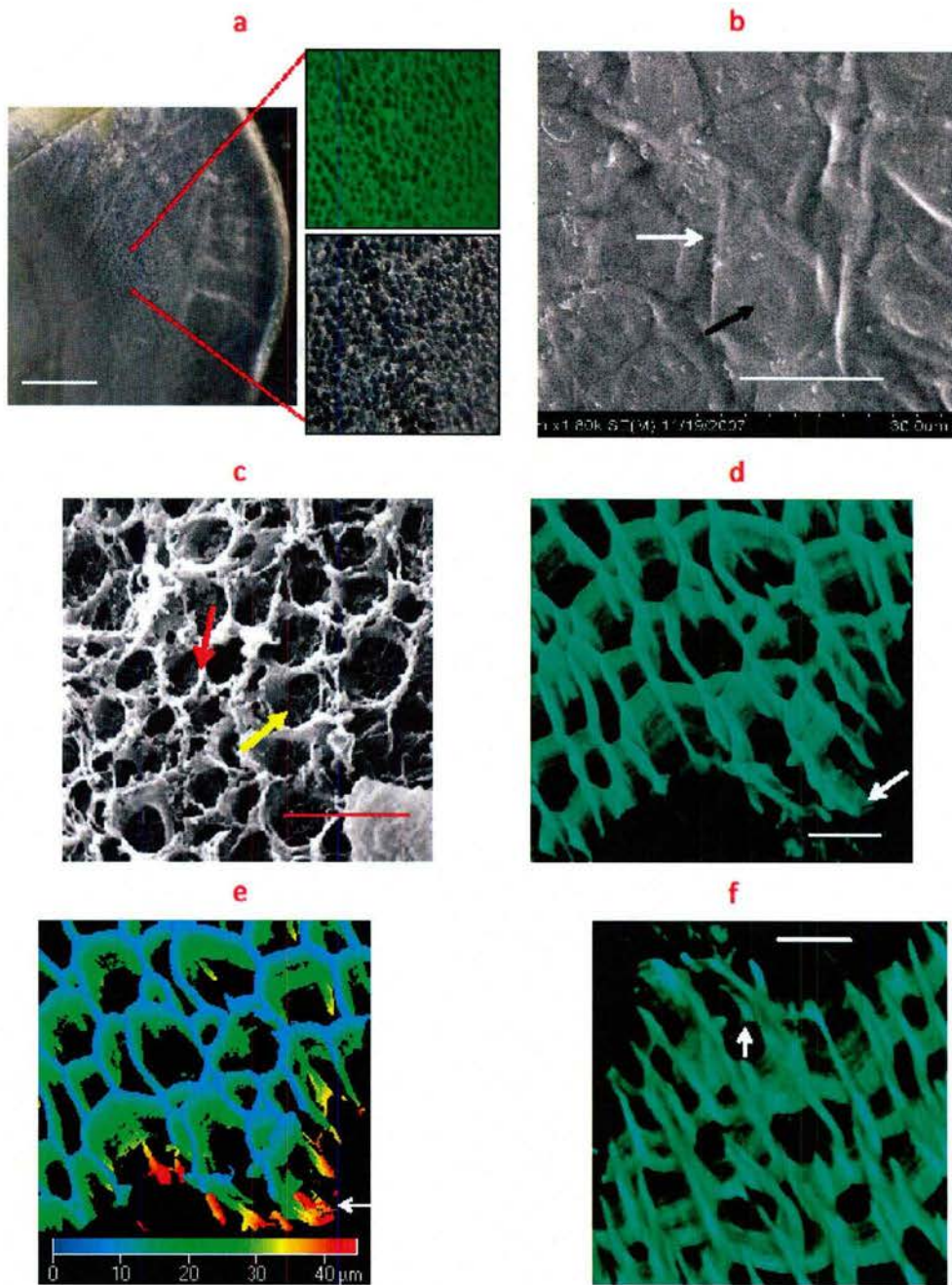


**Figure 1.** Prismatic layer forms on metal implants placed at the shell margin. Prisms form within PMC membranes secreted by the outer mantle epithelial cells. Further descriptions of the images are contained within the text.

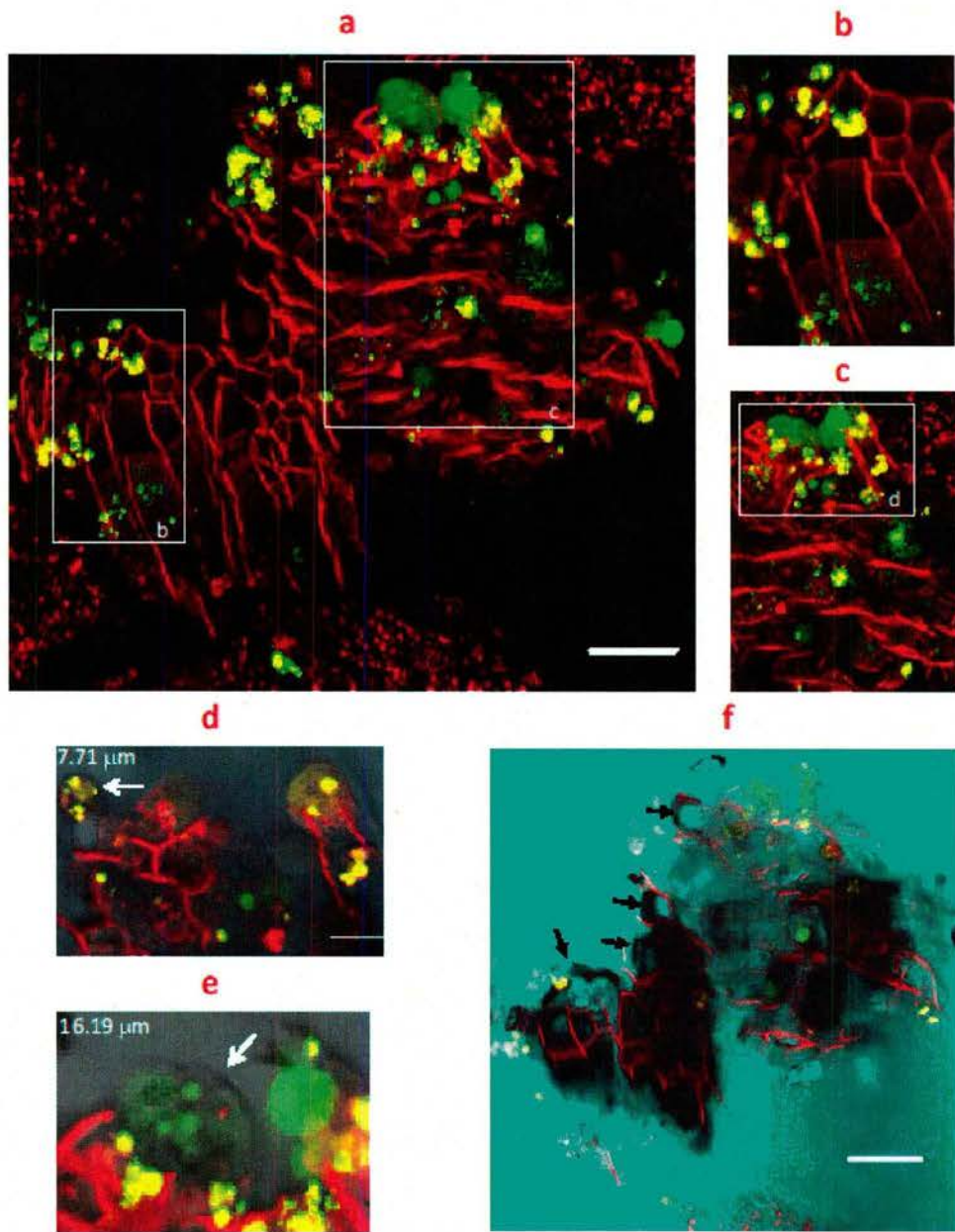


**Figure 2.** Hemocytes deposit crystals and contribute to the PMC membrane during formation of the prismatic layer. Further descriptions of the images are contained within the text.

surface enabling cells to orchestrate the next layer of nanocomposite formation. This explains why membranes are observed between successive folia layers (as shown below) and our observations that inter-prismatic walls are covered with hemocytes.

Using the method of Zaremba et al.,<sup>15</sup> metal alloy discs were placed *in vivo* between the mantle and shell in close proximity to the myostracum, thus promoting the

deposition of folia onto implant surfaces. In Figure 3a, multiple folia layers coat an implant surface. The resulting coating resembles folia formed in natural shell<sup>16</sup> and is comprised of laterally flattened crystal laths (with chevron shaped ends) which fuse to form highly ordered sheets (Fig. 3b, inset from boxed region). We observed that folia layers form on a PMC membrane (red arrow), which acts as a surface. Each folia layer is capped with another membrane (shown here reflected –white arrow) which then acts as the substrate for the next iteration of folia deposition (yellow arrow) (Fig. 3b). A similar multi-lamellar appearance has been reported for nacre<sup>17</sup> and membranes<sup>4</sup> have been observed to occur between and within forming folia laths.<sup>18</sup> We presume that these PMC membranes are of vesicular origin.<sup>19</sup>

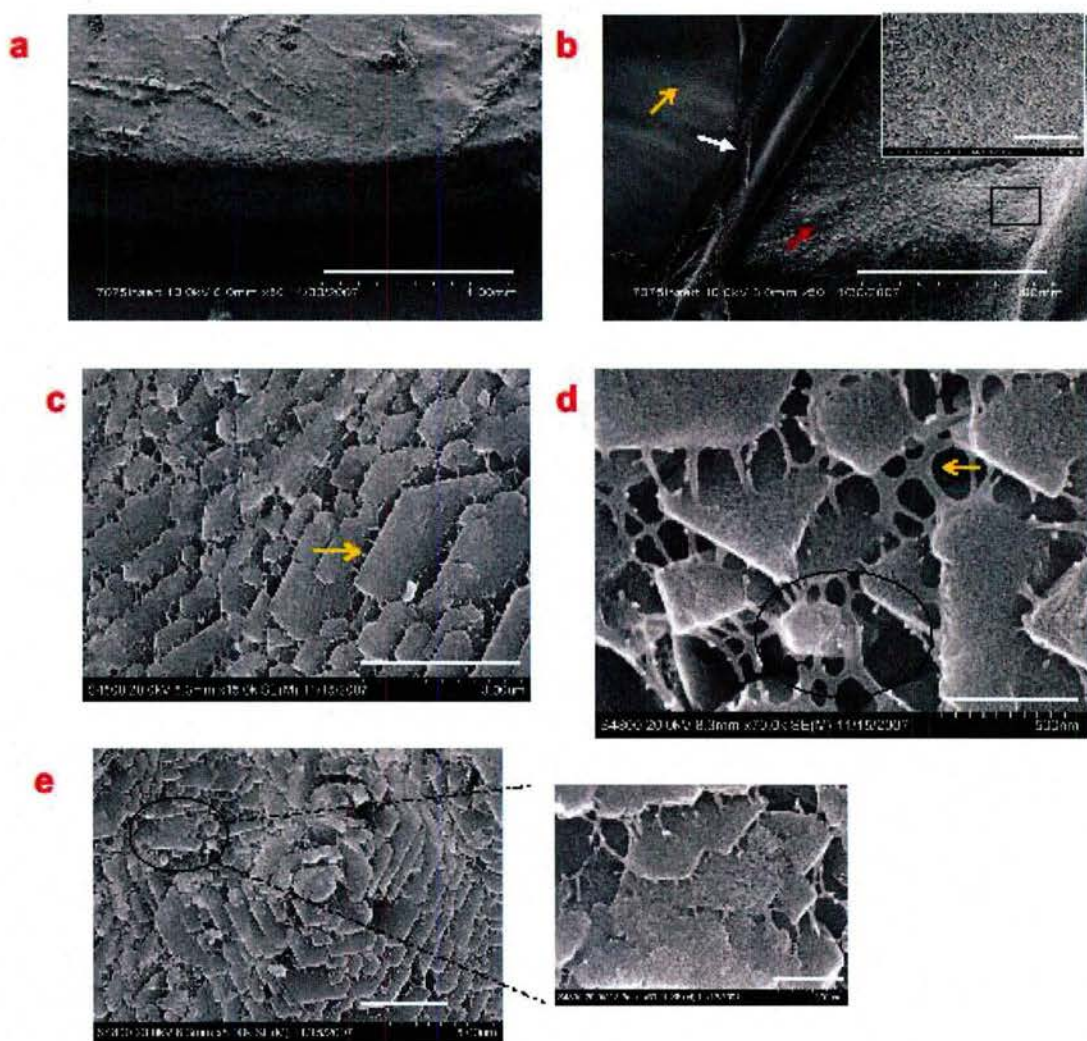


**Figure 3.** Folia form within the PMC on implants placed in vivo. Further descriptions of the images are contained within the text.

Illustrative of simultaneous incorporation of both organic and mineral phases, the SEM study revealed a continuous membranous “web” between folia laths (Fig. 3c, yellow arrow) and among nanocrystals of developing laths (Fig. 3d) all of which become fully incorporated (Fig. 3e, inset). Similar to spider silk, this membrane web is less than 50 nm in diameter and contains a fibrous core distinct from the coating material (Fig. 3d, yellow arrow).<sup>17,20</sup> Moreover, the membrane occurs as a layer through which nanocrystals appear anchored within and may grow and merge to ultimately form a folia lath. Evidence for this is shown in figure 3d where a nanocrystal (circled) is an integral component of the membranous web. This mechanism of crystal growth appears to be analogous to nacre formation.<sup>15,21,22</sup>

Folia formation is initiated by REF cell aggregations which secrete exosome-like vesicles (some containing crystals) that progressively organize into polycrystalline layers. This is consistent with recent observations by Checa et al., which identified lipid bound vesicles that form the surface membrane of gastropod nacre.<sup>19</sup> Folia formation was observed by recovering titanium and aluminum disc implants from the oysters over discrete time intervals. Within 3 hours following implantation, hemocytes infiltrate the area of the implant and adhere to a significant portion of its surface. The cells formed large aggregations (Fig. 4a) and some are refractive granulocytes bearing crystals.<sup>2</sup> After 24 hours, many birefringent crystalline deposits are apparent within these cell masses (Fig. 4b) and, in some cases, large polycrystalline structures are visible (Fig. 4b, top and bottom insets). At this time point, the mineralized mass has lost its previously well-defined cellular appearance which may be a consequence of apoptosis.<sup>23</sup>

After eight days post implantation, unorganized mineral patches cover the entire implant surface (Fig. 4c). Closer inspection of this surface reveals a granular PMC membrane due to the presence of many exosome-like particles that range in diameter from 50 to 500 nm (Fig. 4d). This correlates with the size of vesicles identified on nacre surface membranes and within hemocytes associated with prism PMC walls (Fig. 2). The smaller vesicles (50-100 nm in diameter, white arrow) are embedded in the membrane while larger vesicles, 200 nm and greater (red arrow), occur on its surface. These vesicles aggregate (yellow arrows) to form the mineral patches observed in figure 4a. Several vesicles contain rhomboidal crystals (Fig. 4e) in which the presence of calcium was confirmed by EDS (Fig. 4f).<sup>5</sup> In Figures 4d and 4e, numerous vesicles are shown interacting with each other and the substrate PMC membrane. This interaction may perhaps indicate a form of communication via embedded adhesive domains and signals occurring within the plasma membranes of the exosome-like vesicles, and those of the underlying substrate membrane. The fact that lipids with signaling properties and other cell signaling molecules are components of molluscan shell PMC extracts lends support to this hypothesis.<sup>24-30</sup>

By 28 days, folia occur on most of the implant surface (Fig. 5a). Growth fronts were identified by the presence of mineralized islet structures (100 µm in diameter) which occur on the membranous substrate (Fig. 5b and 5c). These islets grow and fuse to form a confluent folia layer (Fig. 5d). Some of the islet surfaces are unorganized and

granular in appearance (Fig. 5b inset) while others are significantly more organized having well defined crystalline surfaces with growth along a preferred axis (Fig. 5c inset). This pattern of development is consistent with folia formation in natural shell.<sup>16</sup>

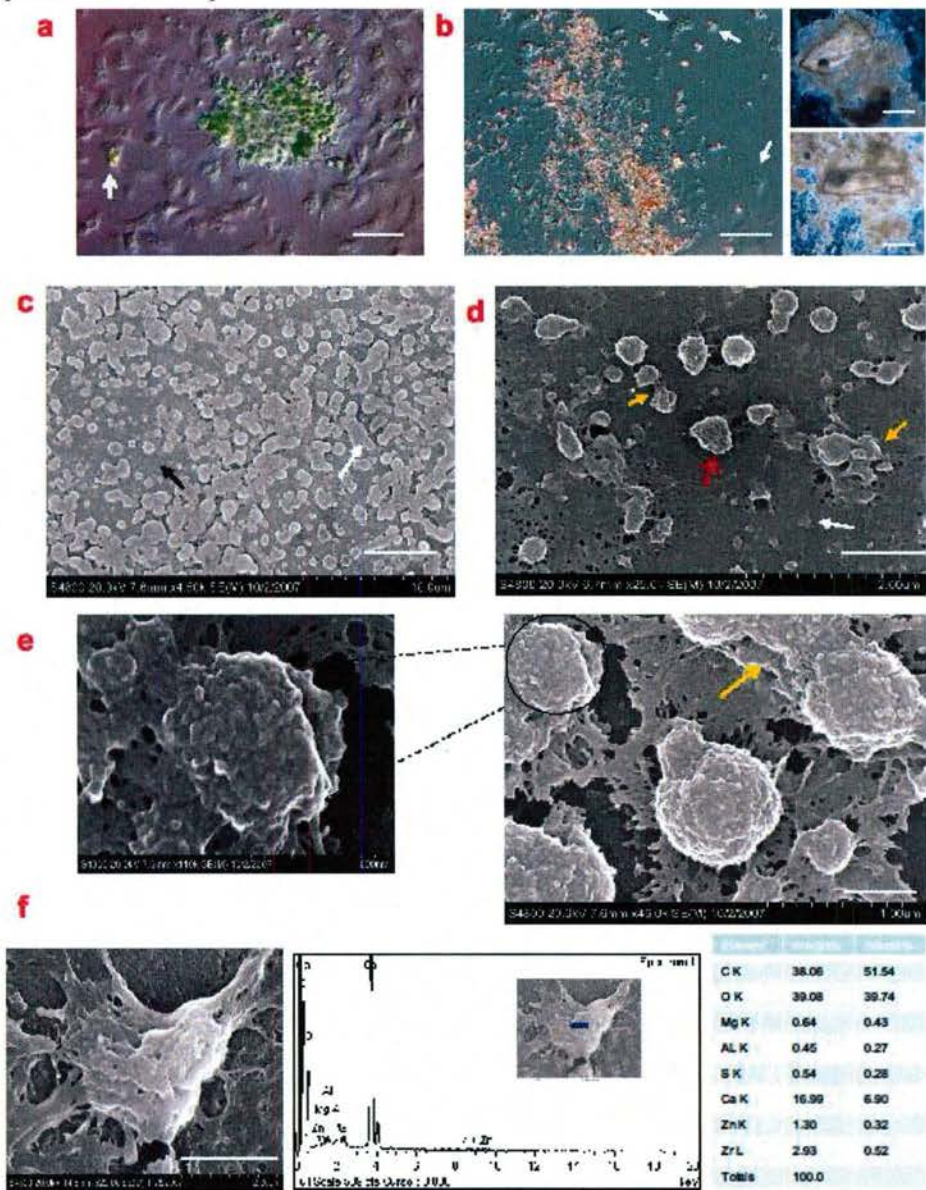


**Figure 4.** Folia formation is initiated by hemocytes depositing vesicular calcite crystals and other exosome-like vesicles onto metal implant surfaces. These vesicles contribute to the PMC. Further descriptions of the images are contained within the text.

Hemocyte activity is apparent on the surfaces of developing folia and may play a role in the maturation of the mineralized layer. In Figure 5b inset, there are numerous large mineral aggregates present on the developing folia islet which are associated with

dendritic organic material (indicated with white arrows), suggesting that the material derives from cells. These structures appear pillar-like and are not yet organized into

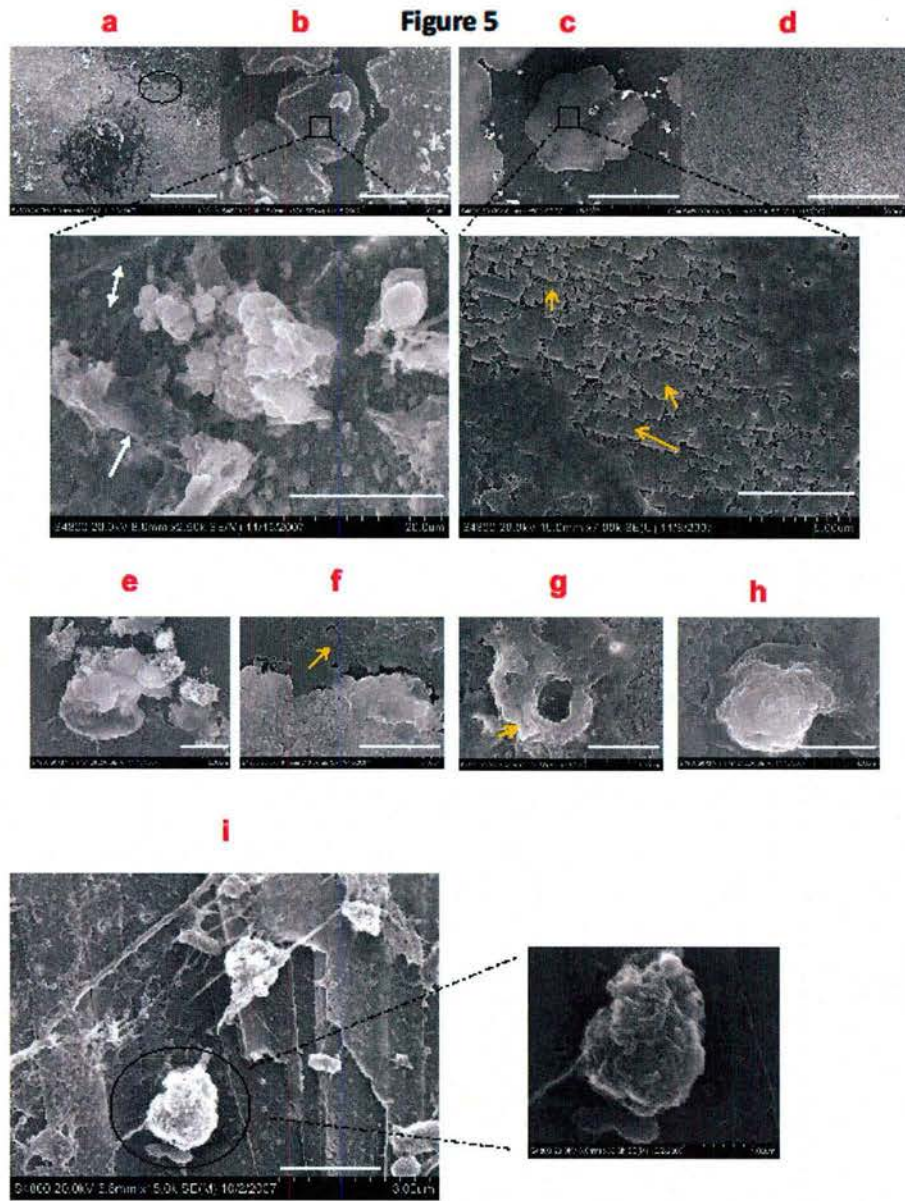


**Figure 5.** Hemocyte activity is evident on developing folia surfaces. Further descriptions of the images are contained within the text.

discernable folia. On the more developed folia surfaces (Fig. 5c inset), lamellapodia-like processes of hemocyte plasma membranes are evident (indicated by yellow arrows).

Hemocyte cells with varying morphologies are observed on developing folia surfaces (Figs. 5e-h). In Fig 5e, the surface of the hemocyte forms pillar-like structures similar in appearance to those identified in Fig.5b inset. An adherent hemocyte is observed at a PMC/folia islet boundary in figure 5f. In figure 5g, an adherent hemocyte contains multiple 500 nm sized vesicles. Figure 5h shows a hemocyte with a bubbled center that has spread on the folia surface. Crystal laden membrane bound vesicles, similar to those observed on 8 day developed folia (Fig. 4d-f), are observed on the surface of fully developed folia laths (Fig. 5i). These particles interact with the folia surface through dendrite-like processes.

In conclusion, we show that the infiltration and cellular activity of hemocytes creates the mineralization front during shell layer formation in oysters. These cells provide both nanocrystals and PMC confined within exo-cytosed vesicles, all of which simultaneously assimilate to form the membranous “web” that we observed in association with the folia laths.<sup>6</sup> Our evidence shows similar hemocyte activity during prism formation. Through cellular orchestrated assembly, a soft PMC phase is produced and laid down as a thin (less than 50 nm) membranous film which encases each intracellularly produced crystal. Lubrication by these films is the key attribute which accounts for the unprecedented nanoscale toughness of shell.<sup>1</sup> The molluscan innovation of simultaneous production of nanocrystals and an instructive PMC by cells provides an unprecedented level of control for the production of hybrid ceramics and accounts for the beautiful hierarchical shell architectures observed in nature.

## METHODS

### *Oyster collection and holding*

Eastern oysters, *Crassostrea virginica* were obtained from Pemaquid Oyster Company Inc. (P.O. Box 302, Waldoboro, Maine 04572). After receipt, the oysters were held in a 180 gallon (681 liter) tank at 18°C in artificial sea water at 31% salinity with saturating levels of dissolved oxygen. The animals were fed twice a week with Shellfish Diet 1800® (Reed Mariculture Inc., 520 McGlincy Lane #1, Campbell, CA 95008). Tank water was continuously filtered except for several hours during feeding. Experimental animals were kept in 50 gallon holding tanks under the same conditions as the acclimation tank.

### *Preparation of metal alloy discs and foils for implantation*

Polished (1µm finish) titanium (Ti6Al4V-grade 5) and aluminum (AA7075-T6) and 316L stainless steel discs (Ti and 316L, Goodfellow Corp., Oakdale, PA; Al, McMaster Carr, Aurora, OH) measuring 12.5 mm in diameter by 1 mm thick were cleaned by a series of 5 minute washes, first in acetone followed by isopropyl alcohol and ending with methanol. The discs were flash dried on a heat block prior to implantation into the oyster. Alternatively, metal alloy foils including titanium (Ti6Al4V), aluminum (AA7075-T6), and 316L stainless steel were also tested.<sup>7</sup> Each foil square measured 1cm<sup>2</sup> by 1 mm thick (Goodfellow Corp., Oakdale, PA). Foil inserts were cleaned and prepared in the same manner as the metal discs.

### *Implantation procedures*

Implantation was accomplished by removing just enough of the shell margin or edge with a diamond saw so that the discs could be inserted into the extrapallial cavity (the region between the mantle tissue and the shell) just inside the most active margin of shell formation. In some cases, the discs were placed deep enough into the extrapallial cavity to come in contact with the adductor muscle region of the mantle. The adductor is the muscle responsible for maintaining valve closure. Implants remained in contact with the shell facing side of the mantle organ throughout the duration of their time of incubation. Implants were collected at 3 h, 24 h, 8 d, 14 d and 28 d intervals. Square foils were placed into a "V" shaped notch was cut into the shell margin using a tile saw with a diamond blade and the foils were glued in place using an ethyl cyanoacrylate based adhesive. Incubations extended up to 14 days. These implants were excised from the shell with a scalpel prior to analysis.

### *Fixation, Imaging and X-ray microprobe (EDS) analysis*

Immediately following removal, implants were viewed on a Nikon AZ-100 microscope using both FITC and epi-polarization channels at low magnification to verify the presence of a mineralized coating. After imaging, the samples were washed for 5 min in 0.2 $\mu$ m filtered seawater. The samples were fixed for one hour in 4% paraformaldehyde 0.1M sodium cacodylate trihydrate buffer at pH 8.0. Following fixation, samples were washed 3X in 0.005M sodium cacodylate trihydrate buffer, pH 8.0 followed by dehydration through a series of ethanol washes starting with 25% ethanol in water, followed by 50, 75, 90 and 100% ethanol for 10 min each. After dehydration, the samples were critically point dried and sputter coated with platinum, and then visualized using a field emission 4800S Hitachi high resolution scanning electron microscope equipped with an Oxford INCA Energy 200 EDS and a GW Electronics Centaurus backscatter detector.<sup>8</sup>

### *Fixation and Imaging of oyster mantle sections*

To obtain mantle tissue sections, live oysters were relaxed by injection of a 1% cocaine solution (dissolved in molluscan PBS) into the adductor muscle. Within 5 minutes the shells would gape, and the animal would be transferred to a cold solution of 10% paraformaldehyde in 0.1M sodium cacodylate trihydrate buffer at pH 8.0. The animal was fixed overnight at 4°C, the hinge ligament was manually opened and the flat valve was excised from the adductor muscle. Fixed relaxed mantle sections were dissected near the growing margin of shell. These sections were washed 3X in 0.005M sodium cacodylate trihydrate buffer, pH 8.0 followed by dehydration through a series of ethanol washes starting with 25% ethanol in water, followed by 50, 75, 90 and 100% ethanol for 10 min per wash. After dehydration, the tissue sections were critically point dried and sputter coated with platinum then visualized using a JEOL 5300 LV scanning electron microscope.

### *Imaging of live prismatic shell formation by epi-fluorescent and laser scanning microscopy*

Notched adult oysters were held overnight in 50 gallon holding tanks. Using a 1.5" 21 gauge sterile needle affixed to a 3 ml sterile plastic syringe, approximately 1 mL of hemolymph was removed from the adductor muscle of the intact animal and transferred

to a 1.5 ml plastic microfuge tube. To fluorescently vital label living hemocytes, 3  $\mu$ M of calcein AM ester (Invitrogen) was added to the tube and incubated for 1 hour at room temperature. The tube bearing the cells was centrifuged at 3,000g (RCF at Tip) for 3 minutes and the supernatant was discarded. The cell pellet was gently re-suspended and washed in molluscan phosphate buffered saline (20mM sodium phosphate, 150 mM or higher NaCl, depending on the osmolality of the holding tank, pH 7.4). The washed and labeled cell suspension was re-injected into the subject oyster's adductor muscle and the animal was replaced into the aquaria. After a 1.5 h incubation, the oyster was relaxed by injection of 1% cocaine solution (dissolved in molluscan PBS) into the adductor muscle. Within 5 minutes the shells would gape, and the hinge ligament was manually opened and the flat valve was excised from the adductor muscle. Live relaxed mantle sections were dissected near the growing margin of shell.<sup>9</sup> To visualize live hemocytes on the growing prismatic layer margin, the shell facing side of the mantle was affixed to a glass cover slip and mounted to a glass slide. These slides were visualized on a Zeiss LSM-510 microscope using the Zeiss Plan Neofluar 40 x oil 1.3 N.A. objective. Confocal stacks using FITC, TRITC and DIC wide field channels were recorded and three dimensional projections obtained using the Zeiss microscope's software. Depth coding (DC), where depth information contained in a sequence (stack) of confocal images is colored coded to represent its z position relative to the volume visualized, was carried out using the Zeiss microscope's software.

## REFERENCES

1. Munch, E., et al. *Science* **322**, 1516-1520 (2008).
2. Mount, A.S., Wheeler, A.P., Paradkar, R.P., and Snider, D. *Science* **304**, 207-300 (2004).
3. Myers, J.M., Johnstone, M.B., Mount, A.S., Silverman, H., and Wheeler, A.P., *Tissue & Cell* **39**, 247-256 (2007).
4. Fleury, C., et al. *Tissue and Cell* **40**, 207-218 (2008).
5. Lowenstam, H.A. and Weiner, S., On biomineralization. 1989: Oxford University Press.
6. Rusenko, K.W., Donachy, J.E., and Wheeler, A.P., eds. Purification and characterization of a shell matrix phosphoprotein from the American oyster. In: Surface Reactive Peptides and Polymers, ed. C.S.Sikes and A.P. Wheeler. 1991, ACS: Washington, D.C. 107-124.
7. Carter, J.G., ed. Shell microstructural data for the Bivalvia. In: Skeletal biomineralization: patterns, processes and evolutionary trends, ed. J.G. Carter. Vol. 1. 1990, Van Nostrand Reinhold: New York. 297-411.
8. Checa, A.G., *Tissue and Cell* 405-416 (2000).
9. Johnstone, M., Ellis, S., and Mount, A. *Journal of Experimental Zoology: Mol Dev Evol* **310B**, 227-239 (2008).
10. Patel, S.V., A novel function of invertebrate collagen in the biomineralization process during the shell repair of eastern oyster, *Crassostrea virginica*. In: Biological Sciences. 2004, Clemson University: Clemson.
11. Franchini, A. and Ottaviani, E., *Tissue and Cell* **32**, 312-321 (2000).
12. Checa, A.G., Esteban-Del, Rodri'guez-Navarro, A.B., and Esteban-Delgado, F., *J. Biomaterials* **26**, 6404-6414 (2005).

13. Carriker, M.R., ed. The shell and ligament. The Eastern oyster, *Crassostrea virginica*. 1996.
14. Keller, S., Sanderson, M., Alexander, S., Stoeck, A., and Altevogt, P., *Immunology Letters* **107**, 102-108 (2006).
15. Zaremba, C.M., et al., *Chem. Mater* **8**, 679-90 (1996).
16. Checa, A.G., Esteban-Delgado, F.J., and Rodriguez-Navarro, A.B., *J of Struct. Biol* **157**, 393-402 (2007).
17. Addadi, L., Joester, D., Nudelman, F., and Weiner, S., *Chem. Eur. J.* **12**, 980-987 (2006).
18. Lee, S.W. and Choi, C.S., *Micron* **38**, 58-64 (2007).
19. Checa, A.G., Cartwright, J.H.E., and Willinger, M.-G. *PNAS* **106**, 38-43 (2009).
20. Marin, F., et al., *J Biol Chem* **280**, 33895-33908 (2005).
21. Lin, A.-M., Chen, P.-Y., and Meyers, M.A., *Acta Biomaterialia* **4**, 131-138 (2008).
22. Yan, Z., et al., *ChemBioChem* **9**, 1093-1099 (2008).
23. Lacoste, A., Cueff, A., and Poulet, S., *J. Cell Sci.* **115**, 761-768 (2002).
24. Rousseau, M., et al., *Comp Biochem Physiol B Biochem Mol Biol* **145**, 1-9 (2006).
25. Farre, B. and Dauphin, Y., *Comp Biochem Physiol B Biochem Mol Biol* (2008).
26. Bédouet, L., et al., *Comparative Biochemistry & Physiology, Part B* **144**, 532-543 (2006).
27. Duplat, D., et al., *Biomaterials* **28**, 4769-4778 (2007).
28. Mourie, L.P., Almeida, M.J., Milet, C., Berland, S., and Lopez, E., *Comp Biochem Physiol B Biochem Mol Biol* **132B**, 217-229 (2002).
29. Sud, D., Doumenc, D., Lopez, E., and Milet, C., *Tissue & Cell* **33**, 154-160 (2001).
30. Zhang, C., Li, S., Zhuojun, M., Liping, X., and Rongqing, Z., *Mar Biotechnol* **2006**, 16972140 (2006).

### Characterization of the Oyster Shell Material as a Bioceramic

(D.C. Hansen, Y.Yoon, K.M. Hansen, UDRI; A.S. Mount, Clemson University)

**Objective:** Characterize the natural bioceramic material in terms of its physical, chemical and electrochemical parameters.

The focus of the current investigation was to determine the physical and chemical composition of layers of natural shell material and to investigate the relationship between the composition of the shell layers and bulk shell electrochemical properties using scanning electron microscopy - energy dispersive spectroscopy (SEM-EDS) and electrochemical impedance (EIS) in a four electrode cell configuration.

The natural bioceramic shell of the Eastern oyster, *Crassostrea virginica*, was investigated to determine its physical and chemical composition using scanning electron microscopy - energy dispersive spectroscopy (SEM-EDS). In addition, resistance and electrolyte conductivity measurements through the shell using electrochemical impedance spectroscopy (EIS) in a four electrode cell configuration were made. The SEM-EDS analysis of oyster shell cross-sections revealed that this multilayered biocomposite material is composed of numerous incongruent "chalky" and "non-chalky" layers, each containing similar chemical elements but having different overall chemical composition

and porosity. SEM analysis revealed that the chalky layers are quite porous and voluminous, whereas the non-chalky layers appear to be non-porous and quite dense and compact. The electrolyte conductivity within the pores of the shell as measured by EIS was shown to be dependent on the ionic concentration of the electrolyte, suggesting that the tortuosity across the shell material via the various chalky and non-chalky layers has an effect on the transport of ions. Rather, consideration of the data in terms of the space charge model indicates that the surface charges within the pores of the shell material facilitate the conduction of ions, much like a ceramic membrane. These findings suggest that the oyster shell may function not only as a protective physical structure, but also as a ceramic membrane allowing for the exchange of ions from the external environment.

The delicate and extremely efficient manner by which natural materials are produced by living organisms during the process of biomineralization is widely recognized as an inspiration for the development of new novel materials because of the unique mechanical properties and sophisticated structures.<sup>1-3</sup> The rigid, mineralized tissues of bones, teeth and seashells can be used for mechanical support, cutting tools and armored protection, respectively, with a great diversity of properties and structures.<sup>1</sup> The unique combination of mechanical properties of these rigid biological materials such as strength, toughness and stiffness make them very attractive as models for the development of synthetic composites.

The shell formation process in molluscs is a promising model for development of bio-inspired ceramics for a wide variety of applications in fields as varied as adaptive surface coatings, corrosion inhibition, hybrid composite materials and more. Molluscan shells are comprised of approximately 98% inorganic CaCO<sub>3</sub> (as calcite and aragonite polymorphs) and 2% organic material (protein, chitin, carbohydrates) arranged in an ordered layered assembly. Organic/inorganic composition and CaCO<sub>3</sub> polymorph vary across molluscan species.<sup>4,5</sup> Recently, a novel mechanism for biomineralization and shell formation in the Eastern oyster (*Crassostrea virginica*) has been elucidated that involves a cellular-mediated crystal-forming process, which indicates that crystal nucleation is intracellular and that hemocytes (circulating blood cells) initiate the shell formation on secreted organic membranes.<sup>6</sup> While advances continue to be made in understanding of the process of crystal nucleation and deposition and resulting shell formation in the phylum Mollusca, interest continues to evolve in the potential applications of this novel bioceramic.

*Physical and Chemical Analyses: SEM and EDS analysis of the oyster shell.* Figure 1, (Top) shows a representative image of a cross-section of an oyster shell which is 7 mm thick and contains several chalky (white) and non-chalky (gray) layers. The bottom image is the area within the box rotated 90 degrees counterclockwise, and shows the non-chalky layers and the chalky layers designated as #2, 5, 7, 8, 11 and #4, 6, 9, 12 respectively. In addition, the outermost layer (#1), innermost layer (#13) and interface layers (#3, 10) are also presented. SEM images (Figure 2) reveal the typical morphology of both the chalky and non-chalky layers. The chalky layers are very porous, as can be seen in both the cross-section image with irregular shapes (Figure 2a) and the top-view

image (Figure 2b). The diameter of the pores can be up to 10  $\mu\text{m}$ . The non-chalky layers seem to have smooth surface and higher density.<sup>7</sup>

EDS analysis indicates that the chemical composition of the oyster shell is mainly composed of C, O and Ca, as expected. The stoichiometric amount of C, O and Ca is to calcium carbonate ( $\text{CaCO}_3$ ).<sup>8</sup> Wheaton reported that the outermost layer of the shell contained occlusions resulting from irritants and impurities, which were incorporated or adsorbed onto the shell.<sup>9</sup> The outermost shell layer also undergoes significant weathering and erosion in the natural environment. The chemical analysis of each oyster layer is summarized in Table 1. While little information is available on the chemical composition of specific shell layers in oysters, report that the porous chalky deposits in *C. gigas*, the Pacific oyster, have higher concentrations of Mg, Na, S, and Cl than the surrounding non-chalky layers.<sup>10</sup> Figure 3 illustrates the carbon + oxygen weight and oxygen/calcium ratio within the different oyster layers. The data were obtained from the EDS elemental analysis of the separate layers. These data suggest that the non-chalky layers have a higher C+O weight and O/Ca ratio than chalky layers. Interestingly, the outermost layer (#1) is more like a chalky layer in terms of C+O weight and O/Ca ratio and the innermost layer (#13) is more like a non-chalky layer. It is known that the chalky layers of oysters are quite porous, are of lower density, and have a higher weight percent of organic material (hence less mineral content) than non-chalky layers.<sup>11-13</sup> Our observation of crystalline NaCl at the interface layer between non-chalky and chalky layers may reflect a concentration of ions in ambient seawater at the time the interface layer was forming. While the interface layers had significant amounts of Na and Cl, the C+O weight % was lower in comparison to non-chalky layers and is similar to the C+O weight % of the chalky layers. Indeed the interface may be a transition stage between non-chalky and chalky layer formation.

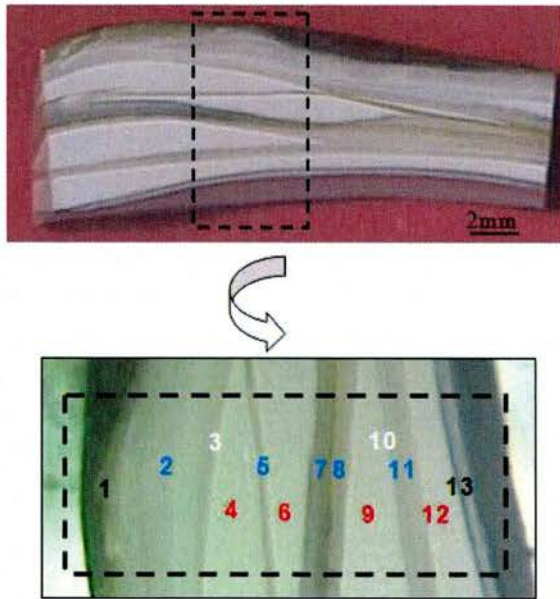
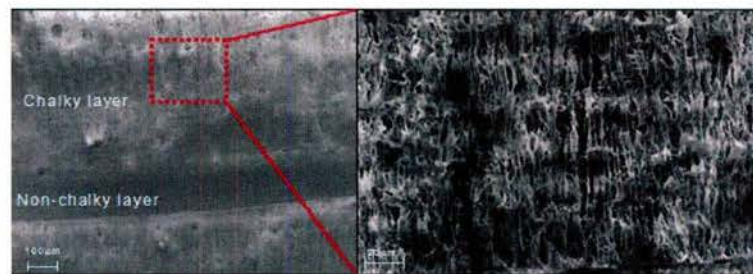


Figure 1. Cross section images of oyster shell material. The thickness of the shell was 7 mm with different layers (Non-chalky layers: #2, 5, 7, 8 and 11; Chalky layers: #4, 6, 9 and 12. Interface layers: #3 and 10; Innermost layer: #13)



(a) Cross-view



(b) Top-view

Figure 2. Scanning electron micrographs of the oyster shell with (a) cross section image illustrating chalky and non-chalky layers; (b) top-view image of chalky layer

Notation	#	(wt %)							
		C	O	Na	Mg	Al	Si	Cl	Ca
Outermost layer	1	14.2	27.8			5.7	3.6		48.7
Non-chalky layer	2	18.6	40.5	0.7					40.3
	5	15.9	38.4	1.1					44.6
	7	17.0	39.1	0.6	0.4				42.9
	8	19.0	39.3	0.8			1.0		39.9
	11	16.7	38.6	1.0					43.7
Chalky layer	4	12.4	34.1	0.5	0.5				52.5
	6	14.1	38.0	0.7					47.2
	9	12.3	34.1	0.5	0.4				52.7
	12	11.8	29.6		0.5			0.7	52.5
Interface	3	21.5	22.7	12.8			13.7		29.3
	10	16.7	12.9	22.0			25.1		23.3
Innermost layer	13	18.6	40.1	0.5					40.0

Table 1. EDS Chemical analysis of oyster shell material.

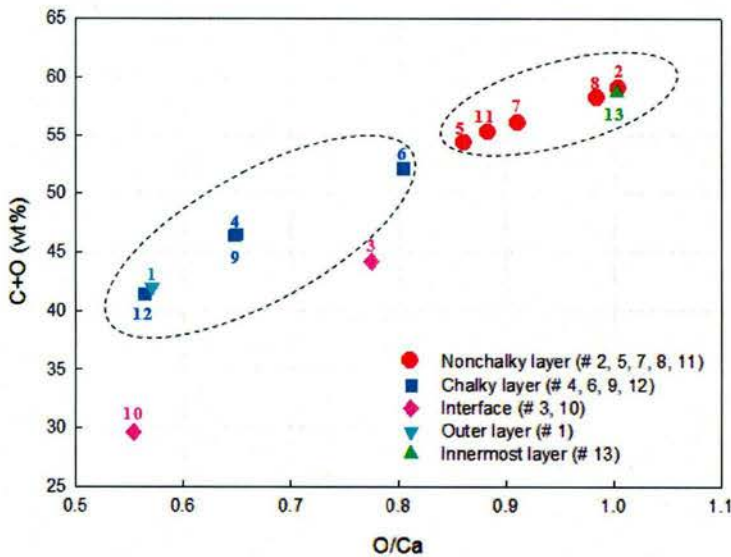


Figure 3. Carbon + oxygen weight % (C+O) plotted as a function of the oxygen/calcium ratio (O/Ca) in the different oyster shell layers.

#### *Resistivity through oyster shell.*

Electric charges on the surfaces of porous membranes play an important role in the electrolyte transport process and ion flux across the membrane itself.<sup>14</sup> More specifically, transport through a charged capillary pore can be described by the space charge model.<sup>15</sup> In general, it considers straight pores of uniform cylindrical shape carrying a uniformly distributed charge, however it has been validated in the case of a ceramic microporous membrane that is a tortuous medium having pores with size distributions and no well-defined geometry.<sup>16</sup>

The resistance measurement using EIS to obtain information regarding the membrane and pore resistance of porous materials has been described previously.<sup>16-18</sup> The present resistance measurements carried out with an intact, porous oyster shell serving as a membrane between two cells allows one to obtain the overall resistance of the electrochemical cell,  $R_{cell}$ . For these numerical calculations, the membrane is assumed to be composed of parallel cylindrical pores having an identical mean radius; while this does not accurately describe the oyster shell, it does provide a first approximation for the estimation of the flow of solute and solvent through the material. If the resistance of the solution,  $R_{sol}$ , in the electrochemical cell is known, then it is possible to obtain the membrane resistance,  $R_m$  by the following relationship:<sup>16</sup>

$$R_{\text{cell}} - R_{\text{sol}} = R_m \quad (1)$$

The electrolyte conductivity within the pores of the membrane material,  $\lambda_{\text{pore}}$  can then be determined from resistance measurements using the following relation:<sup>16</sup>

$$\lambda_{\text{pore}} = \frac{\lambda^h R_m^h}{R_m} \quad (2)$$

where  $\lambda^h$  is the conductivity of the electrolyte at high salt concentration,  $R_m^h$  is the resistance across the pores of the when the cell is filled with the high salt solution, and  $R_m$  is the resistance across the pore when the cell is filled with the measurement solution.

Electric charges on the surfaces of porous membranes play an important role in the electrolyte transport process and ion flux across the membrane itself.<sup>10</sup> More specifically, transport through a charged capillary pore can be described by the space charge model.<sup>11</sup> In general, it considers straight pores of uniform cylindrical shape carrying a uniformly distributed charge, however it has been validated in the case of a ceramic microporous membrane that is a tortuous medium having pores with size distributions and no well-defined geometry.<sup>12</sup>

The resistance measurement using EIS to obtain information regarding the membrane and pore resistance of porous materials has been described previously.<sup>12-14</sup> The present resistance measurements carried out with an intact, porous oyster shell serving as a membrane between two cells allows one to obtain the overall resistance of the electrochemical cell,  $R_{\text{cell}}$ . For these numerical calculations, the membrane is assumed to be composed of parallel cylindrical pores having an identical mean radius; while this does not accurately describe the oyster shell, it does provide a first approximation for the estimation of the flow of solute and solvent through the material. If the resistance of the solution,  $R_{\text{sol}}$ , in the electrochemical cell is known, then it is possible to obtain the membrane resistance,  $R_m$  by the following relationship:<sup>12</sup>

$$R_{\text{cell}} - R_{\text{sol}} = R_m \quad (1)$$

The electrolyte conductivity within the pores of the membrane material,  $\lambda_{\text{pore}}$  can then be determined from resistance measurements using the following relation:<sup>12</sup>

$$\lambda_{\text{pore}} = \frac{\lambda^h R_m^h}{R_m} \quad (2)$$

where  $\lambda^h$  is the conductivity of the electrolyte at high salt concentration,  $R_m^h$  is the resistance across the pores of the when the cell is filled with the high salt solution, and  $R_m$  is the resistance across the pore when the cell is filled with the measurement solution.

Resistance data for each of the sequential immersions of the oyster shell are presented in Table 2. The resistance of the oyster shell during 5 days immersion in 3.5 wt% NaCl solution was acquired at 10 mHz during the EIS scan. During the 5 day

NaCl concentration	$R_{cell}$ ( $\Omega$ )	$R_{sol}$		$R_m$ ( $\Omega$ )	$\lambda_{pore}$ (mS)
		$\lambda_0$ (mS)	Resistance ( $\Omega$ )		
3.5 wt%	11805.7	55.2	18.1	11787.6	1656.1
Deionized water	215141.7	0.291	3436.4	211705.2	92.2
$5.8 \times 10^{-4}$ wt%	233948.5	0.138	7246.4	226702.1	86.1
1 wt%	228401.4	20.5	48.8	228352.6	85.5
5 wt%	241033.2	81.0	12.3	241020.8	81.0
3.5 wt% later	126974.4	43.2	23.1	126951.3	153.7

Table 2. Resistance values of cell, solution, membrane and conductivity of solution and pores of the oyster shell in 3.5 wt%, deionized water,  $5.8 \times 10^{-4}$  wt%, 1.0 wt%, 5.0 wt% and 3.5 wt% NaCl solutions.

immersion, the resistivity through the oyster shell was measured as  $11,805 \Omega$ , reaching a steady state after approximately 40 hours. This is notable, since the measured resistance of the solution with a conductivity meter was  $18.1 \Omega$  (55.2 mS), This value agrees with published values,<sup>19</sup> indicating that the resistance values being measured in the 4-electrode cell configuration were across the oyster shell. Using the relationship in Equation (1) the membrane resistance of the oyster shell was calculated to be  $11,787 \Omega$  (Table 2). It can be seen that due to the relatively small values for the solution resistance ( $R_{sol}$ ) in all of the cases, the membrane resistance ( $R_m$ ) is very similar and approximates that of the cell resistance ( $R_{cell}$ ). In order to measure the  $R_{cell}$  in a different solution, the solution was changed without changing the configuration of the shell or the electrodes. After the 3.5% NaCl solution was removed from both cells and replaced with the deionized water (DW) and immersed for two days, the  $R_{cell}$  during the initial 12 hours of immersion remained similar in value to that of the previous immersion measurement. The  $R_{cell}$  values for the initial 12 hours reflect the resistance of the 3.5% NaCl that was still contained within the shell. After the initial 12 hours, the  $R_{cell}$  resistance increased, indicating that transport of the ions of the more conductive electrolyte from the pores out of the shell into the bulk solution had occurred, causing an increase in the overall cell resistance by more than one order of magnitude. The resistance then stabilized to  $215,141 \Omega$  after approximately 40 hours. The resulting  $R_m$  calculated was  $211,705 \Omega$  (Table 2).

In looking at the values presented in Table 2, the  $R_{cell}$  measured in sequential immersions of  $5.8 \times 10^{-4}$  wt%, 1 wt%, 5 w% and 3.5 wt% NaCl solutions for one day each respectively shows that for each of these solutions, there was little or no change in the  $R_m$  calculated for the oyster shell after the initial immersion in 3.5 wt% NaCl, even though the  $R_{sol}$  decreased for each succeeding electrolyte. The values plotted in Figure 4 are the average resistance values over the length of each solution immersion. For all measurements, the oyster shell sample and the cell configuration was identical with only the solution being changed. It is interesting to note that the  $R_m$  values for the succeeding

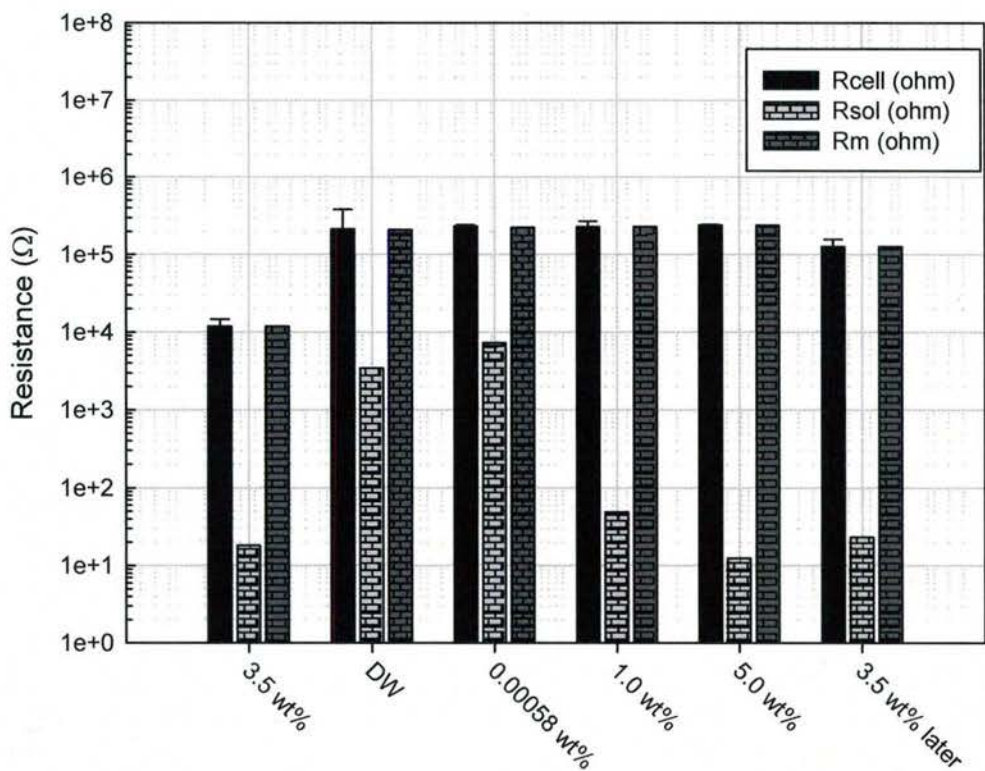


Figure 4. The average cell, solution and membrane resistance values of the oyster shell material for the sequence of immersions in 3.5% NaCl and deionized water.

NaCl solutions following the DW immersion did not decrease, although there was a slight decrease noted for the final immersion in 3.5% NaCl for 24 hours. These results suggest that the rate of diffusion of the electrolyte (or the migration of the ions) through the shell material was fairly constant after the DW immersion; this is evidenced by the very small variation in the  $R_m$  values between each solution.

Comparison measurements were made using a polyethersulfone filter (140  $\mu\text{m}$  thin and a 0.45  $\mu\text{m}$  pore size) in an identical cell set up. The  $R_{cell}$  in 3.5 wt% NaCl solution was 68.4  $\Omega$ ; this value is somewhat higher than the  $R_{sol}$  itself (23.6  $\Omega$ ), indicating that the  $R_m$  was 44.8  $\Omega$ . The  $R_{cell}$  and  $R_{sol}$  in DW were 12,426.7  $\Omega$  and 3,154.6  $\Omega$ , respectively. The  $R_m$  in the DW was calculated as 9,272.1  $\Omega$ . After changing the solution to 3.5 wt% NaCl solution, the  $R_{cell}$  and  $R_m$  were again 73.8  $\Omega$  and 58.2  $\Omega$ , respectively, being very close to the values obtained with the first immersion in 3.5% NaCl. This result indicates that the membrane resistance of the filter is strongly dependent on the concentration of the solution. This is in contrast to the oyster shell data in Figure 4, where the membrane resistance is independent from the solution ion concentration. The diameters of the pores in the polyethersulfone filter are an order of

magnitude smaller than the pores in the oyster shell, indicating that the relative size of the pores can not account for the observed differences.

Figure 5 and Table 3 show the average  $R_{cell}$  values, the measured  $R_{sol}$  and calculated  $R_m$  of the glass ceramic filter which had 10~16  $\mu\text{m}$  pore size similar to the pore size of the oyster shell as shown in Figure 2. Similar to the previous immersion tests, these results indicate that the solution resistance was comparatively small in contrast to the measured  $R_{cell}$  values, again resulting in the  $R_m$  values approximating the  $R_{cell}$  values. Also, the  $R_{cell}$  and  $R_m$  values remain constant with decreasing solution concentration, except for the 0.87 wt% NaCl immersion and the final immersion in 0.22 wt% NaCl, where the  $R_{cell}$  values decreased markedly. There is no clear explanation for these two

NaCl concentration	$R_{cell}$ ( $\Omega$ )	$R_{sol}$		$R_m$ ( $\Omega$ )	$\lambda_{pore}$ (mS)
		$\lambda_0$ (mS)	Resistance ( $\Omega$ )		
3.5 wt%	23358.0	54.8	18.2	23339.8	54.8
1.75 wt%	23182.1	30.4	32.9	23149.2	55.3
3.5 wt%	25072.9	55.1	18.1	25054.7	51.0
0.87 wt%	7747.3	17.1	58.3	7688.9	166.3
3.5 wt%	24853.3	76.7	13.0	24840.2	51.5
0.44 wt%	25969.6	10.5	95.1	25874.4	49.4
3.5 wt%	26532.6	77.0	12.9	26519.6	48.2
0.22 wt%	905.1	5.8	173.0	732.1	1747.0

Table 3. Resistance values of cell, solution, membrane and conductivity values of solution and pores of the glass ceramic filter in series of NaCl immersion solutions

immersion conditions resulting in a decrease in the  $R_{cell}$  and  $R_m$  values. However, this decrease of the  $R_m$  may be related to the conductivity inside the pore and the bulk solution.

Using the relationship in Equation (2) the conductivities inside the pore and the bulk solution of the glass ceramic filter were calculated. The pore resistance and conductivity measured with the high salt solution (3.5 wt% NaCl) are 23,339.8  $\Omega$  and 54.8 mS, respectively, for the first electrolyte immersion (Table 3). In general, it appears that the pore conductivities within the glass ceramic membrane are not strongly dependent on the solution concentration; the pore conductivities inside the glass ceramic filter at 0.87 wt% and 0.22 wt% NaCl slightly increased. This data does not consider the effect of the conductivity of the bulk solution, just the NaCl concentration. However, the ratio of the pore conductivity ( $\lambda_{pore}$ ) to the bulk solution conductivity ( $\lambda_0$ ) at the various lower solution concentrations indicates that the conductivities inside the pores at these concentrations were consistently higher than those of the bulk solution (i.e. greater than unity) and *dependent on* the bulk solution concentration. Figure 6 shows the conductivity ratio between the pore and the bulk solution ( $\lambda_{pore}/\lambda_0$ ) of the glass ceramic filter as a function of electrolyte concentration. It is clear that there is a bulk solution concentration

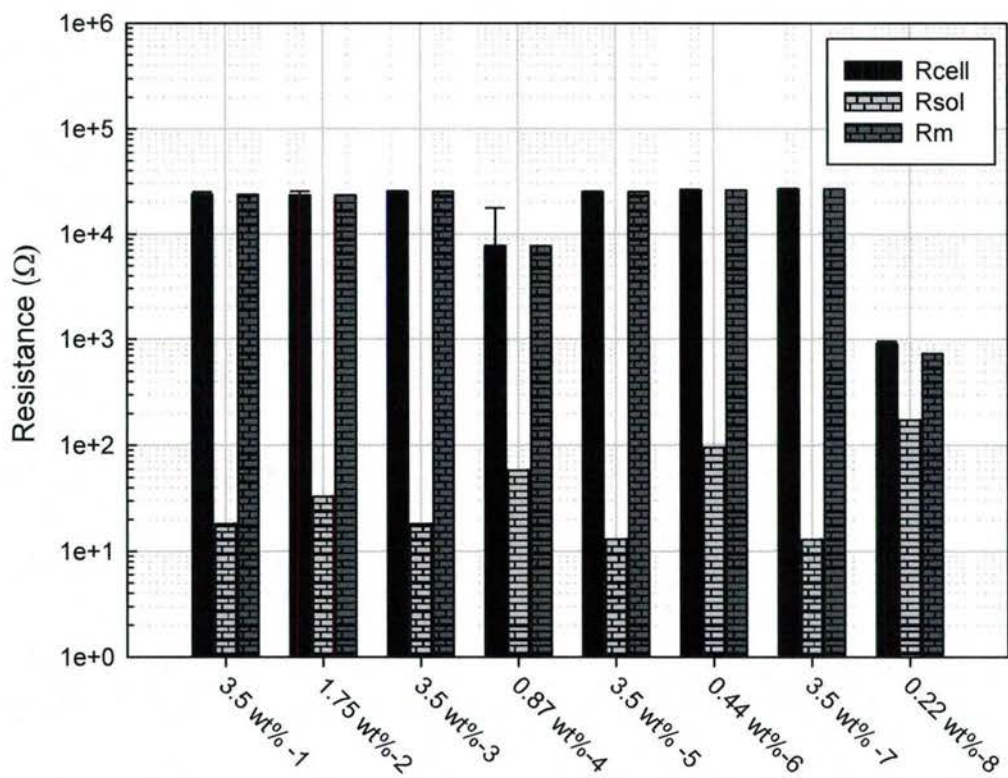


Figure 5. The average cell, solution and membrane resistance values of the ceramic membrane material for the sequence of immersions in 3.5% NaCl.

effect on the *conductivity ratio of the pore and the bulk solution*, which indicates that the conductivity inside the pores is indeed dependent upon the NaCl concentration in the bulk. This enhanced conductivity inside the pores at each bulk concentration may be due to the charged surface on the pore wall. This can occur due to the balancing by counterions, which can lead to an increase in surface conductance that can drive the pore conductivity to be greater than the bulk solution conductivity.<sup>12</sup> This higher conductivity inside the pore decreases as the NaCl concentration increases while decreasing the

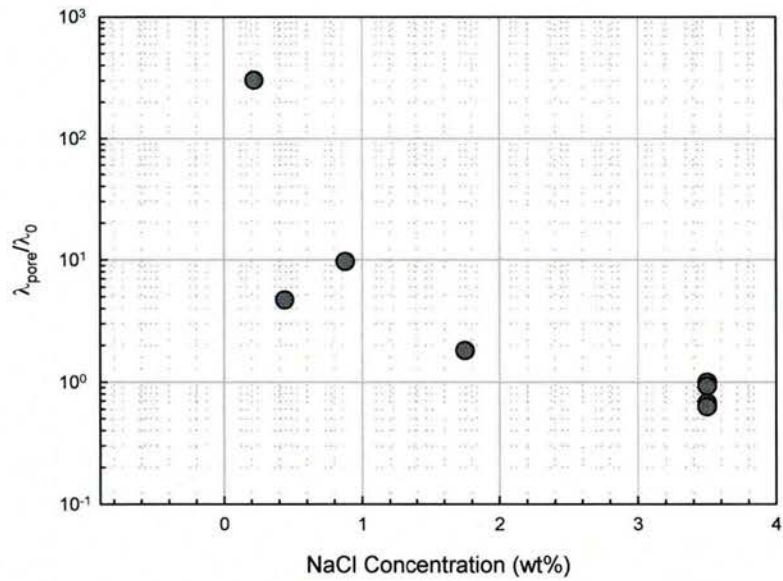


Figure 6. The variation of the ratio  $\lambda_{\text{pore}}/\lambda_0$  of the glass ceramic filter as a function of NaCl solution.

charged surface of the membrane. At 3.5 wt% NaCl the ratio is close to unity which indicates that the conductivity inside the pores is similar to that of the bulk solution.

Figure 7 presents the conductivity ratio between the pore and the bulk solution ( $\lambda_{\text{pore}}/\lambda_0$ ) of the oyster shell as a function of bulk solution concentration in DW,  $5.8 \times 10^{-4}$  wt%, 1.0 wt%, 3.5 wt% and 5.0 wt% NaCl solutions. The ratio of the pore/bulk solution conductivities for the oyster shell demonstrates that the conductivities inside the pores were consistently higher than those of the bulk solution, except for the highest concentration solution. This result indicates that the ionic conductivity of the oyster shell is similar to that of the glass ceramic filter.

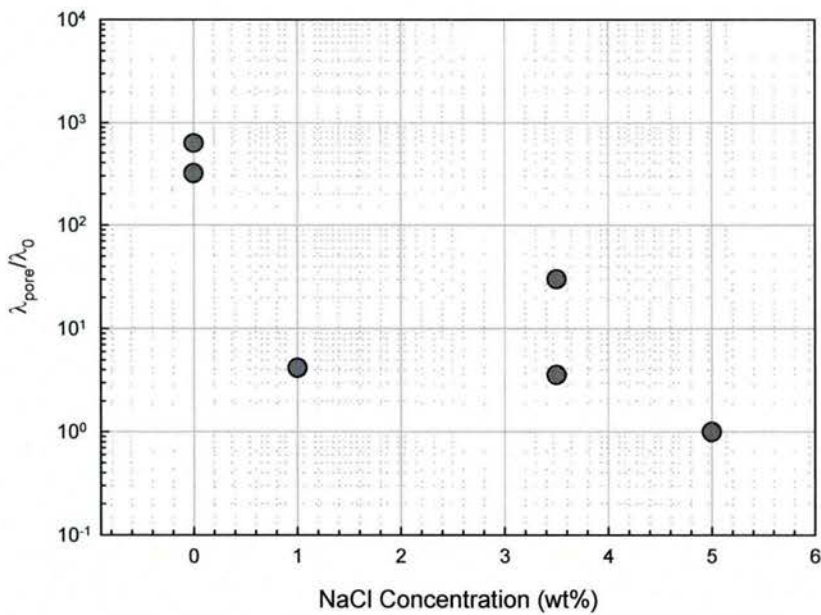


Figure 7. The variation of the ratio  $\lambda_{\text{pore}}/\lambda_0$  of the oyster shell material as a function of NaCl solution.

The resistance measurements on the oyster shell in this study were not carried out with different ceramic materials or ionic solutions for comparison; however the results presented are consistent in showing that the pore conductivities of the oyster shell are somewhat dependent on the bulk solution concentration. This suggests that there may be an effect of the tortuous shell structure on the transport of ions or a blocking effect of some salt precipitation inside the porous structure.<sup>20</sup> As the  $R_m$  values for the oyster shell were consistently high ( $> 2 \times 10^5$  Ohms) after the immersion in the DW, with no apparent bulk solution effect, this suggests that there may have been an irreversible change in the pore wall surface charge. The observation that the pore conductivities were consistently higher than the bulk solution conductivities after the DW immersion appears to support this hypothesis.

Consideration of the conductivity data in terms of the space charge model indicates that the surface charges within the pores of the shell material facilitate the conduction of ions similar to that observed for the ceramic membrane. The ability of the shell material to act as an ion conductor in combination with its unique physical and chemical composition makes it an attractive bioceramic for a variety of applications where a naturally derived and environmentally friendly porous membrane is required.

## METHODS

**Materials and chemical analysis.** Market quality Eastern oysters (*Crassostrea virginica*) were obtained from a commercial supplier (Pemaquid Oyster Co. Waldoboro, Maine) and

maintained in a recirculating seawater system at 21 parts per thousand (ppt) salinity and 65° F. Oysters were shucked, tissues removed, and shells scrubbed clean. The shells were allowed to dry for at least 1 week at ambient room temperature and relative humidity prior to sectioning with a ceramic tile saw. The composition and morphology of each layer was analyzed using energy dispersive spectroscopy (EDS, Genesis 2000) and scanning electron microscopy (SEM, Zeiss EVO-50XVP) respectively. Prior to SEM/EDX analysis on the shells, samples were polished by grinding on 1200 grit SiC paper and rinsed with deionized water of 18 MΩ·cm resistivity.

*Four electrode resistance measurement.* Intact oyster shells (i.e. no sectioning or grinding was done) were used for these measurements. The whole shell was positioned in between two independent Flat Cells (Model K0235, Princeton Applied Research) on either side of the shell. To compare the oyster shell with other materials, a 140 μm thin polyethersulfone filter (Supor®-450, Pall Corp.) with a 0.45 μm pore size and a 2 mm thick glass ceramic filter with a pore size range of 10~16 μm diameter (Adams & Chittenden Sci. Glass) were used. Two saturated calomel reference electrodes were positioned in each cell with one connected to the sense electrode and the other connected to the reference electrode to precisely control voltage across the shell. A pair of platinum mesh electrodes were used to apply and measure the current, *i.e.* working and counter electrodes, respectively (Figure 8). The exposed surface area of the oyster shell was 1.0 cm<sup>2</sup>. The concentration of the NaCl electrolyte was the same in both cells for each measurement but was then replaced with NaCl solutions of varying concentrations in both cells to determine the resistivity across the oyster shell by using a four electrode resistance measurement (Gamry Reference 600 Potentiostat/Galvanostat/ ZRA) electrochemical impedance spectroscopy (EIS). The EIS measurement was carried out with 15 mV amplitude from 10<sup>5</sup> to 0.01 Hz at Open Circuit Potential (OCP). The electrolyte solutions used ranged from 5.0 wt% through 3.5 wt% NaCl to deionized water. The volume of each electrolyte in each cell was 300 ml. All solutions were prepared with deionized water of 18 MΩ·cm resistivity. Changing of the electrolyte in both cells was accomplished by removing the solution and then immediately filling with the new solution. The resistance of the each solution was measured using a conductivity meter (Orion 105A+, ThermoElectron Corp.).

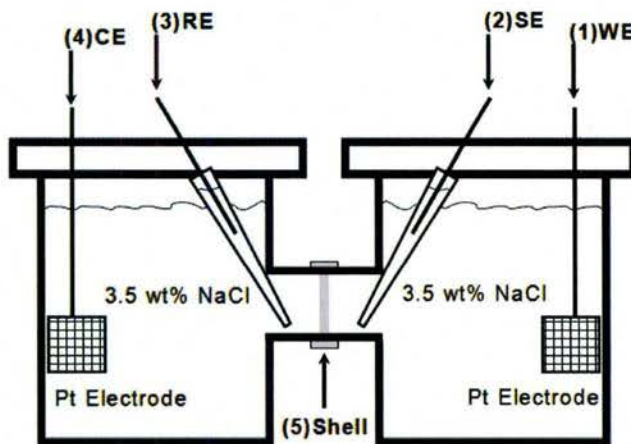


Figure 8. Cell configuration for the four electrode resistance measurement through the oyster shell. (1) Working electrode, (2) Sense electrode, (3) Reference electrode, (4) Counter electrode, and (5) oyster shell.

## REFERENCES

1. F. Barthelat, *Phil. Trans. R. Soc. A*, **365**, 2907 (2007).
2. F. Barthelat, H. Tang, P.D. Zavattieri, C.-M. Li, and H.D. Espinosa, *J. Mech. Phys. Solids*, **55**, 306 (2007).
3. N. Nassif, N. Pinna, N. Gehrke, M. Antonietti, C. Jager, and H. Colfen, *PNAS*, **102**, 12653 (2005).
4. I. Kobayashi and T. Samata, *Mat. Sci. Eng. C*, **26**, 692 (2006).
5. N. Watabe. *The Mollusca*, ed. E.R.T.a.M.R. Clarke, NY: Academic Press. 69 (1988).
6. A.S. Mount, A.P. Wheeler, R.P. Paradkar, and D. Snider, *Science*, **304**, 297 (2004).
7. M. Takenaka, M. Ikeda, and S. Terada, *Anal. Commun.*, **36**, 109 (1999).
8. B. Pokroy and E. Zolotoyabko, *J. Mater. Chem.*, **13**, 682 (2003).
9. F. Wheaton, *Aquacultural Engineering*, **37**, 3 (2007).
10. K. Wada and S. Suga, *Nat. Pearl Res. Lab.*, **20**, 2219 (1976).
11. M.R. Carriker, R.E. Palmer, and R.S. Prezant, *Proc. Nat. Shell. Assoc.*, **70**, 139 (1980).
12. P. Korringa, *Proc. Calif. Acad. Sci.*, **27**, 133 (1951).
13. S. Weiner and L. Hood, *Science*, **190**, 987 (1975).

14. A. Szymczyk, P. Fievet, M. Mullet, J.C. Reggiani, and J. Pagetti, *J. Mem. Sci.*, **143**, 293 (1998).
15. G.B. Westermann-Clark and J.L. Anderson, *Journal of The Electrochemical Society*, **130**, 839 (1983).
16. A. Szymczyk, P. Fievet, B. Aoubiza, S. C., and J. Pagetti, *J. Mem. Sci.*, **161**, 275 (1999).
17. P. Fievet, A. Szymczyk, B. Aoubiza, and J. Pagetti, *J. Mem. Sci.*, **168**, 87 (2000).
18. E. Mueller, C.S. Sikes, and B.J. Little, *Corrosion (Houston, TX, United States)*, **49**, 829 (1993).
19. L. Dzib-Perez, J. Gonzalez-Sanchez, J.M. Malo, and F.J. Rodriguez, *Anti-Corrosion Methods and Materials*, **56**, 18 (2009).
20. R.M. Souto, M.M. Laz, and R.L. Reis, *Biomaterials*, **24**, 4213 (2003).

### **Thermal Conductivity Determination of Oyster Shell Material**

(D.C. Hansen, UDRI; Andrey Voevodin and Sabyasachi Ganguli, Air Force Research Laboratory)

**Objective:** Characterize the natural oyster shell material for its thermal conductivity properties.

Natural shell specimens were measured to determine their thermal conductivity. Shell samples from natural oysters were ground and polished on both the inside and outside aspect of the shell samples to make them as flat as possible. These inside and outside samples were cut into 10 mm squares for the thermal property measurements. Bulk thermal diffusivity was measured using a Netzsch Laser flash apparatus under nitrogen purge. The laser flash technique allows measuring the thermal diffusivity ( $h$ ) of solid materials over a temperature range -180°C to 2000°C. The laser flash (or heat pulse) technique consists of applying a short duration (< 1ms) heat pulse to one face of a parallel sided sample and monitoring the temperature rise on the opposite face as a function of time. This temperature rise is measured with an infrared detector. A laser is used to provide the heat pulse. A thermal diffusivity ( $h$ ) can then be calculated as

$$h = \frac{\pi L^2}{\pi t_{1/2}} \quad [1]$$

where  $\pi$  is a constant,  $L$  is the thickness of the specimen and  $t_{1/2}$  is the time for the rear surface temperature to reach half it's maximum value. Heat capacity of the shell was measured by a differential scanning calorimeter. Weight and dimensions of the samples were accurately measured to calculate the density of the samples by taking a ratio of the measured weight to measured volume. Finally, with the measurements of the heat

capacity, the density and the thermal diffusivity, the thermal conductivity ( $k$ ) of the samples can be obtained as

$$k = C_p \rho h \quad [2]$$

All the measurements for heat capacity, density, and diffusivity were measured at 25°C. The results of the thermal property measurements are presented in Figures 1 and 2.

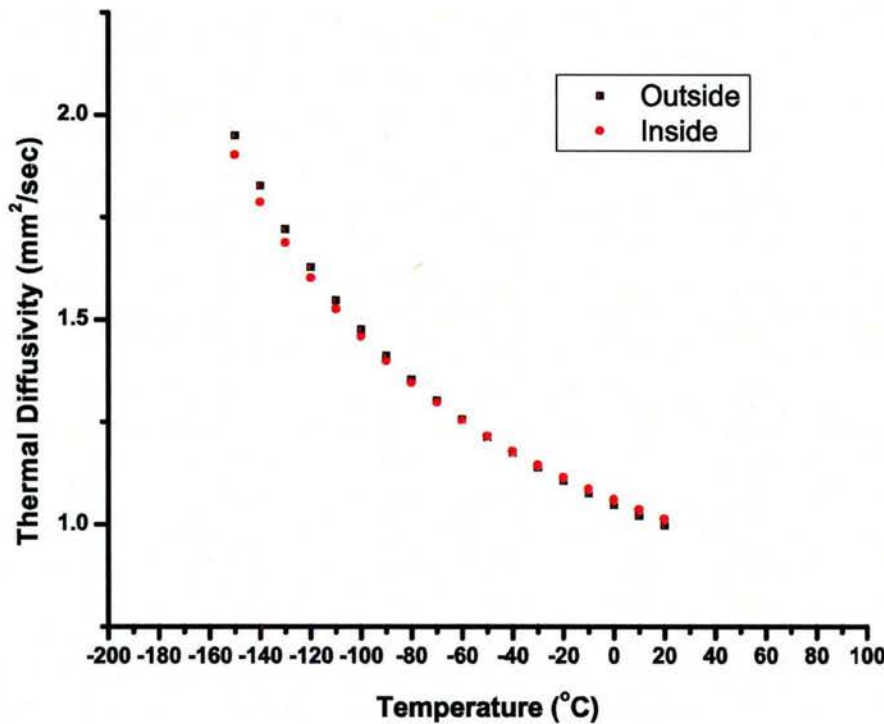


Figure 1. Thermal diffusivity vs. temperature plot for the natural oyster shell material.

There was no difference in the thermal transport properties between the inside and outside aspect shell specimens. The surface finish of the shells was very rough in spite of the polishing and this would affect the thermal transport property. The heat capacity measurements were performed on TA Q1000 modulated DSC which is capable of measuring up to -70°C. The rest of the subambient heat capacity data was obtained by extrapolation.

For shells the heat conduction is essentially by phonons alone. The simple theory of lattice heat conduction gives,

$$k = \frac{1}{3} C_v T v^2$$

Where

$k$  = Thermal Conductivity

$C_v$  = Specific heat at constant volume

$\tau$  = Phonon relaxation time which is the average time between two successive phonon scattering events.

$v$  = Phonon velocity

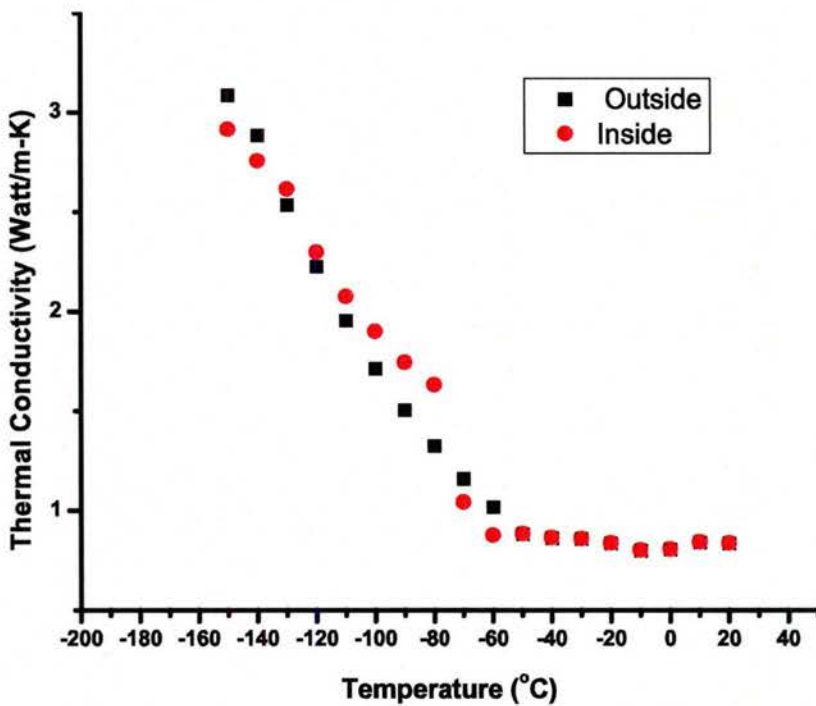


Figure 2. Thermal conductivity vs. temperature plot for the natural shell.

Therefore the entire physics of thermal conductivity is contained essentially in the understanding of various phonon scattering processes. There are many mechanisms for phonon scattering, such as phonon-phonon scattering, phonon-electron scattering, and the scattering of phonons by crystal boundaries and defects. At normal temperatures in pure crystals the phonon-phonon scattering is the dominant scattering mechanism and it is caused by the anharmonicity in the interatomic potential energy function.

The temperature dependence of the thermal conductivity gives a unique insight into the relative contributions of various phonon relaxation mechanisms, because different mechanisms have different temperature dependencies.

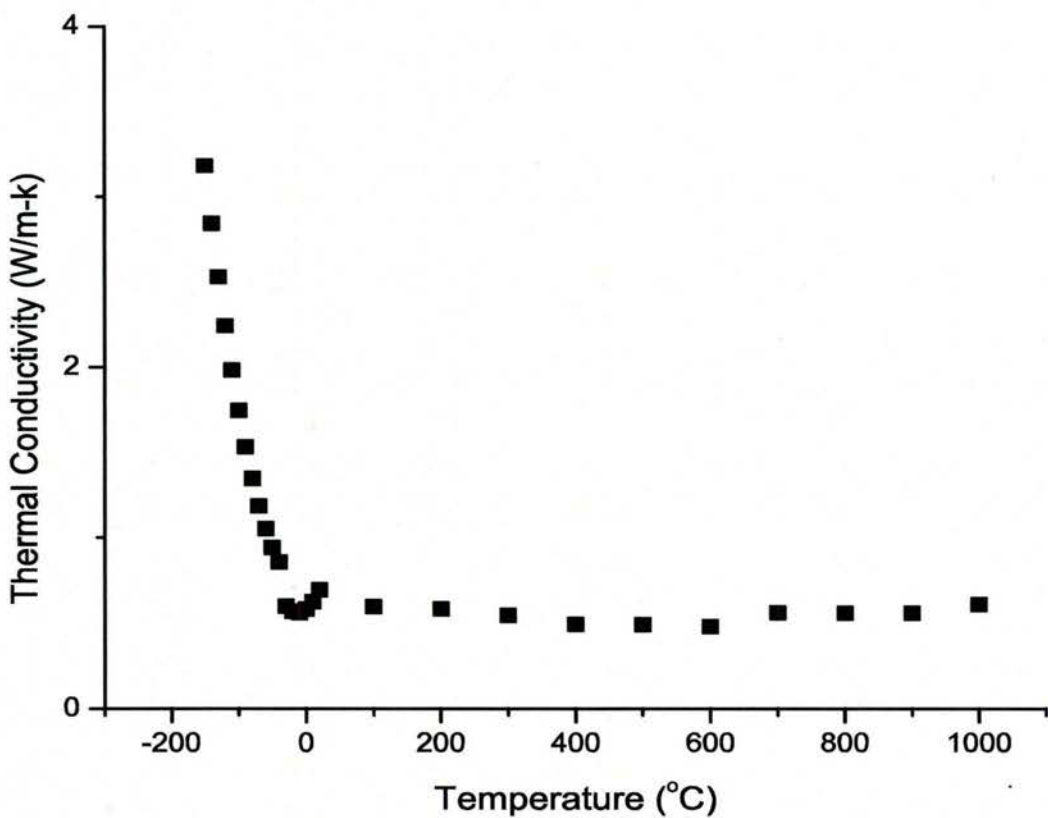


Figure 3. Thermal conductivity vs. temperature plot for the outside aspect of natural oyster shell.

The change in thermal transport of the shells due to the change in temperature could be explained from the Debye temperature dependence on thermal transport. Debye temperature is a measure of the stiffness of the crystal. Above  $T_{\text{Debye}}$  all modes are getting excited, and below  $T_{\text{Debye}}$  modes begin to be frozen out. Thus below  $T_{\text{Debye}}$  the phonon velocity increases and this raises the thermal transport in the material. At high temperatures above  $T_{\text{Debye}}$ , Umklapp processes result in a very large reduction in the heat current and thus thermal conductivity decreases.

A second set of measurements were made up to 1000 °C. The data are presented in Figure 3. As can be seen, the oyster shell material acts as an insulator from approximately -80 °C to 1000 °C. This indicates that the oyster shell material have thermal conductivity properties between that of glass and aluminum oxide.<sup>1</sup>

These results indicate that the natural oyster shell material has some thermal properties which may have some high temperature applications as a barrier coating or in high temperature fuel cells as a membrane, due to its ionic conductivity properties.

## REFERENCES

1. CRC Handbook of Chemistry and Physics, D.R. Lide, Ed. 77<sup>th</sup> Edition (1996-1997).

**Personnel Supported:**

University of Dayton  
Research Institute (UDRI)

Staff/Faculty:

Douglas C. Hansen Ph.D.  
Karolyn M. Hansen, Ph.D.

Yuhchae Yoon, Ph.D.

UDRI Students:

Eric Griesenbrock (undergraduate)  
Kelly Wedell (undergraduate)

Clemson University

Staff/Faculty:

Andrew S. Mount, Ph.D.  
Mary Beth Johnstone, Ph.D.  
Joshua Mount

**Publications:**

1. Johnstone, M.B., K.M. Hansen, N.V. Gohad, D.C. Hansen and A.S. Mount, "Cellular Orchestrated Biominerization of Nanocrystalline Composites on Metal Alloys," *Nature Materials* (2009) under review.
2. Yoon, Y., A.S. Mount, K.M. Hansen and D.C. Hansen, "Electrolyte Conductivity Through the Shell of the Eastern Oyster Using a Four Electrode Measurement," *J. Electrochem. Soc.* (2009) submitted.

**Interactions/Transitions:**

Technical Presentations:

1. M.B. Johnstone, K.M.. Hansen, N.V. Gohad, D.C. Hansen, and A.S. Mount. "Towards Biomimetic Ceramic Coatings: Cellular Aspects of Oyster Shell Biominerization.' National Shellfisheries Association Annual Meeting, Savannah GA, March 22-26, 2009.
2. M.B. Johnstone, M.E Staton, C. Saski, and A.S. Mount. 'A Bioinformatics Approach for Discovering Shell Matrix Proteins.' National Shellfisheries Association Annual Meeting, Savannah GA, March 22-26, 2009.
3. A.S. Mount, N.V. Gohad, M.B. Johnstone, K.M. Hansen, and D.C. Hansen. 'The Mineralization Front of the Eastern Oyster is Cellular.' National Shellfisheries Association Annual Meeting, Savannah GA, March 22-26, 2009.
4. Y. Yoon, A.S. Mount, D.C. Hansen, and K.M. Hansen. 'Assessment of Oyster Shell Structural Properties for the Development of 'Green' Composite Materials.' National Shellfisheries Association Annual Meeting, Savannah GA, March 22-26, 2009.
5. K.M. Hansen, A.S. Mount and D.C. Hansen (2008). "Nucleation and Growth of Ceramic Films on Metallic Surfaces." 214<sup>th</sup> Meeting of The Electrochemical Society, Honolulu, HI.

6. Y. Yoon, A.S. Mount, K.M. Hansen and D.C. Hansen (2008). "Electrochemical Characterization of Natural Oyster Shell as a Corrosion Inhibiting Coating Material." 214<sup>th</sup> Meeting of The Electrochemical Society, Honolulu, HI.
7. A. S. Mount, K.M. Hansen and D.C. Hansen (2007). "Scanning Kelvin Probe Characterization of Hemocyte Deposited Ceramic Films on Metallic Surfaces." 212<sup>th</sup> Meeting of The Electrochemical Society, Washington, DC.
8. (Invited) A.S. Mount (2007), "The Materials Science of Biology: From Fundamental Research to Practical Applications," University of Texas Biology Department.
9. A.S. Mount (2007), "Biofouling and Cellular Biomineralization of Marine Invertebrates," Supercomputer O7 Reno, Nevada.

**New Discoveries, Inventions or Patent Disclosures:**

1. "DEPOSITION OF NANOCRYSTALLINE CALCITE ON SURFACES BY A TISSUE AND CELLULAR BIOMINERALIZATION," A.S. Mount, N.V. Gohad, D. C. Hansen, K.M. Hansen and M.B. Johnstone. Provisional Patent Filed 4 December 2008.

**Honors/Awards:**    **None.**